Simulating growth of TDP-43 cytosolic inclusion bodies in neuron soma

Andrey V. Kuznetsov

Department of Mechanical and Aerospace Engineering, North Carolina State University,

Raleigh, NC 27695-7910, USA; e-mail: avkuznet@ncsu.edu

Abstract

This paper introduces a mathematical model for the growth of TDP-43 inclusion bodies. The model's equations make it possible to determine numerically the concentrations of TDP-43 dimers, monomers, and aggregates. Assuming that all aggregates integrate into the inclusion bodies, the model predicts the size of TDP-43 inclusion bodies. In the scenario where protein degradation machinery is dysfunctional, resulting in infinite half-lives for TDP-43 dimers, monomers, and aggregates, an approximate solution of the model equations is derived. This solution, valid for large times, predicts that the inclusion body's radius increases proportionally to the cube root of time. To the author's knowledge, this study presents the first attempt to model the relationship between the size of TDP-43 inclusion bodies and time. The sensitivity analysis of the approximate solution indicates that the concentrations of TDP-43 monomers and aggregates, as well as inclusion body radii, are independent of the kinetic constants. However, the approximate solution becomes invalid for the scenario with physiologically relevant (finite) half-lives of TDP-43 dimers, monomers, and aggregates. In contrast to the situation with infinite half-lives, for various values of kinetic constants, the curves representing concentrations of monomers and aggregates, as well as the curves depicting inclusion body radii, converge to distinct constant values.

Keywords neuron; amyotrophic lateral sclerosis; frontotemporal lobar degeneration; Finke-Watzky model; mathematical modeling

Abbreviations

ALS amyotrophic lateral sclerosis

F-W Finke-Watzky

FTLD frontotemporal lobar degeneration

1. Introduction

The presence of TDP-43 inclusion bodies stands out as a pathological hallmark in amyotrophic lateral sclerosis (ALS) and frontotemporal lobar degeneration (FTLD) diseases [1-4]. ALS is distinguished by the gradual decline of motor neurons, resulting in skeletal muscle weakness and, ultimately, fatality within a span of 3 to 5 years [5,6].

TDP-43, a nuclear, intrinsically disordered, soluble protein [7,8] with a molecular weight of 43 kDa [9], is synthesized in the cytoplasm, and in healthy neurons, it predominantly resides in the nucleus [10-12]. Degradation of TDP-43 occurs through both proteasomal and autophagy pathways [13]. However, in TDP-43 proteinopathies, this protein undergoes mislocalization from the nucleus to the cytoplasm [14,9], forming TDP-43 inclusion bodies characterized by ubiquitinated and hyper-phosphorylated variants of TDP-43 [3].

Under pathological conditions, TDP-43 undergoes a conversion from its native dimeric state [15] to a monomeric form. This transformation results in TDP-43 mislocalization from the nucleus to the cytoplasm, where it forms irreversible, amorphous aggregates [16,5]. Subsequently, these aggregates grow into inclusion bodies. Notably, the nature of these inclusion bodies, whether they exhibit toxicity or act in a neuroprotective manner by sequestering toxic soluble oligomers, remains uncertain [1,14]. There is a possibility that TDP-43 pathology spreads between neurons through a prion-like mechanism [2,17].

This paper develops a model for TDP-43 inclusion body growth, predicting the correlation between the radius of the inclusion body and time. This builds upon my previous research, which explored the growth of amyloid-β plaques [18] and Lewy bodies [19,20]. The goal is to apply the methodology developed in [18,20] to simulate the growth of TDP-43 inclusion bodies.

2. Materials and models

2.1. Governing equations

According to [5], the initial stage of TDP-43 aggregation involves the monomerization of TDP-43 dimers:

$$D \xrightarrow{k_M} 2M \ . \qquad (1)$$

To simulate TDP-43 aggregation, a phenomenological two-step Finke-Watzky (F-W) model, as described in [21,22], was employed. The F-W model, which has been successfully applied to fit experimental data on neurological protein aggregation [21], simulates polymer aggregation through two pseudoelementary,

parallel, and competing processes: continuous nucleation and autocatalytic surface growth [23]. The F-W model is characterized by the following transitions:

$$M \xrightarrow{k_1} B\,, \tag{2}$$

$$M + B \xrightarrow{k_2} 2B\,. \tag{3}$$

The mathematical model is derived by making three conservation statements for dimers, monomers, and aggregates. The model utilizes time, *t*, as the sole independent variable, with the dependent variables listed in Table 1 and parameters summarized in Table 2.

The conservation of TDP-43 dimers in the soma is expressed by the following equation:

$$\frac{d[D]}{dt} = \frac{q_D}{V_{soma}} a_{21} - k_M [D] - [D] \frac{\ln(2)}{T_{1/2,D}}\,. \tag{4}$$

In Eq. (4), $a_{21} = 10^{21} \frac{\mu\text{M}\ \mu\text{m}^3}{\text{mol}}$ represents the conversion factor from $\frac{\text{mol}}{\mu\text{m}^3}$ to μM. The first term on the right-hand side of Eq. (4) simulates the rate at which TDP-43 dimers, which is a native form of TDP-43, are produced in the soma. The second term is formulated by applying the law of mass action to describe the rate of reaction in Eq. (1). The third term simulates the degradation of TDP-43 dimers due to their finite half-life.

The conservation of TDP-43 monomers in the soma is described by the following equation:

$$\frac{d[M]}{dt} = 2k_M [D] - k_1 [M] - k_2 [M][B] - [M] \frac{\ln(2)}{T_{1/2,M}}\,, \tag{5}$$

where the first term on the right-hand side describes the generation of TDP-43 monomers through their conversion from dimers. The second term simulates the decrease of monomer concentration resulting from their transformation into the misfolded active form capable of autocatalysis. In the F-W model, this process is conceptualized as a nucleation process (refer to Eq. (2)). The third term accounts for the decrease of monomer concentration due to autocatalytic conversion into their aggregated form (refer to Eq. (3)). The fourth term represents the degradation in TDP-43 monomers due to their finite half-life.

By expressing the conservation of TDP-43 aggregates, the following is derived:

$$\frac{d[B]}{dt} = k_1 [M] + k_2 [M][B] - [B] \frac{\ln(2)}{T_{1/2,B}}\,. \tag{6}$$

The first and second terms on the right side of Eq. (6) simulate the generation of TDP-43 aggregates resulting from their production from monomers through nucleation and autocatalytic processes, respectively. The fourth term on the right side represents the decline of TDP-43 aggregates due to their limited half-life. The existing model does not simulate the mechanism of sticky TDP-43 aggregates coming together to form the inclusion bodies. It is presumed that this assembly process occurs more rapidly than the formation of TDP-43 aggregates in the soma.

Eq. (4)-(6) are solved with the following initial conditions:

At $t = 0$: $\quad [D] = [D]_0, \quad [M] = 0, \quad [B] = 0.$ (7a,b,c)

Table 1. Dependent variables in the model.

Symbol	Definition	Units
$[B]$	Molar concentration of misfolded form of TDP-43 prone to aggregation	μM
$[D]$	Molar concentration of TDP-43 dimers, representing the native form of TDP-43	μM
$[M]$	Molar concentration of TDP-43 monomers	μM
r_{IB}	Radius of the growing inclusion body, assuming it takes on a spherical form	μm

Table 2. Model parameters along with their estimated values.

Symbol	Definition	Units	Value or range	Reference or estimation method	Value(s) used in computations
a_{21}	Conversion factor from $\frac{\text{mol}}{\mu\text{m}^3}$ to μM	$\frac{\mu\text{M}\ \mu\text{m}^3}{\text{mol}}$	10^{21}		10^{21}
$[D]_0$	Initial concentration of TDP-43 dimers	μM			0 [a]

D_{soma}	Diameter of the soma	μm	20 [b]		20
D_{IB}	Diameter of a mature spherical TDP-43 inclusion body	μm	1-25 μm [c]	[24]	8
k_1	Rate constant associated with the first pseudoelementary step in the F-W model that describes the nucleation of the misfolded form of TDP-43 prone to aggregation	s^{-1}			10^{-4} , 10^{-6} , 10^{-8} [d]
k_2	Rate constant associated with the second pseudoelementary step of the F-W model that describes the autocatalytic growth of misfolded form of TDP-43 prone to aggregation	μM^{-1} s^{-1}			10^{-4} , 10^{-6} , 10^{-8} [e]
k_M	Rate constant associated with the reaction that describes the conversion of TDP-43 dimers into monomers	s^{-1}			10^{-2} , 10^{-4} , 10^{-6} [f]

MW	Molecular weight of TDP-43 monomer	g mol^{-1}	4.3×10^{4} [g]	[9,12,25]	4.3×10^{4}
N_A	Avogadro's number	mol^{-1}	6.022×10^{23}		6.022×10^{23}
N_{IB}	Number of mature TDP-43 inclusion bodies within the soma (assumed to be of the same volume)		0-4 [h]	[1]	2
q_D	Rate at which TDP-43 dimers are generated within the soma	mol s^{-1}	6.68×10^{-23}	Estimated using Eq. (20)	6.68×10^{-23}
$t_{IB,f}$	Duration of TDP-43 inclusion body growth	s	1.26×10^{8} [i]	[3,5,13,6]	1.26×10^{8}
$T_{1/2,B}$	Half-life of TDP-43 in misfolded form prone to aggregation	s	8.64×10^{4} - 1.73×10^{5} [j]	[3]	1.30×10^{5}, 10^{20} (to simulate $T_{1/2,B}\to\infty$)
$T_{1/2,D}$	Half-life of TDP-43 dimers	s	4.32×10^{4} [k]	[26,3]	4.32×10^{4}, 10^{20} (to simulate $T_{1/2,D}\to\infty$)
$T_{1/2,M}$	Half-life of TDP-43 monomers	s	4.32×10^{4} [l]	[26,3]	4.32×10^{4}, 10^{20} (to simulate $T_{1/2,M}\to\infty$)
ρ_{IB}	Density of TDP-43 inclusion bodies	g/μm^3	1.35×10^{-12} [m]	[27]	1.35×10^{-12}

[a] Since a continuous production of TDP-43 dimers was assumed in the model, the initial concentrations of dimers become less significant over extended periods of time.

[b] A representative neuron with a soma diameter of 20 μm was considered.

[c] Mature spherical TDP-43 inclusions vary in diameter from 1 to 25 μm, while skein-like inclusions have diameters ranging from 0.5 to 1.0 μm and lengths extending up to 15 μm [24].

[d] As there is a lack of published data on the kinetic rates in the F-W model describing the aggregation of TDP-43 protein, three representative values, 10^{-4}, 10^{-6}, 10^{-8} s^{-1}, were selected for k_1 based on information presented in [21] for various proteins (summarized in Table S1).

[e] Due to the absence of published data on the kinetic rates in the F-W model describing the aggregation of TDP-43 protein, three representative values, 10^{-4}, 10^{-6}, 10^{-8} μM^{-1} s^{-1}, were selected for k_2 based on information presented in [21] for various proteins (summarized in Table S1).

[f] Given that the half-life of the first-order reaction involved in TDP-43 monomerization (refer to Eq. (1)) is on the order of hours [5], and the rate constant of a first-order reaction is $k_M = 0.693 / T_{1/2}$, three representative kinetic rates, 10^{-2}, 10^{-4}, 10^{-6} s^{-1}, were employed to simulate potential rates of the TDP-43 monomerization reaction.

[g] A mass of TDP-43 monomer is 43,000 dalton [9,12,25].

[h] Number of TDP-43 inclusion bodies is taken from Fig. 8C in [1].

[i] In cases of ALS, patients typically succumb to the disease within 2–5 years from the onset of symptoms [3,5,13,6]. It is probable that the growth of TDP-43 inclusion bodies commenced even before the manifestation of the disease symptoms. Consequently, a growth duration of 4 years was assumed for the inclusion bodies, after which the neuron undergoes cell death.

[j] Given that the stability of TDP-43 increases in mutations (24-24 hours versus 12 hours for the wild type [3]), it was hypothesized that the half-life of the misfolded form of TDP-43 is 2-4 times longer than that of the wild-type TDP-43.

[k] The reported half-life of wild-type TDP-43 is 12 hours [26,3]. Given that native TDP-43 exists in a dimeric form [16], this half-life was attributed to TDP-43 dimers.

[l] A same half-life of 12 hours was assumed for both TDP-43 monomers and TDP-43 dimers.

[m] A commonly employed density value that remains consistent across different protein types is 1.35 g/cm³ [27].

2.2. Approximate analytical solution for the scenario when $T_{1/2,D} \to \infty$, $T_{1/2,M} \to \infty$, and $T_{1/2,B} \to \infty$

The approximate analytical solution is derived for a scenario where the protein degradation machinery is impaired, resulting in infinitely long half-lives for TDP-43 dimers, monomers, and aggregates. Assuming that the concentration of TDP-43 dimers is at steady state, the solution to Eq. (4) is as follows:

$$[D] = \frac{1}{k_M} \frac{q_D}{V_{soma}} a_{21} . \tag{8}$$

Adding Eqs. (5) and (6) yielded the following result:

$$\frac{d[M]}{dt} + \frac{d[B]}{dt} = 2 \frac{q_D}{V_{soma}} a_{21} . \tag{9}$$

Integrating Eq. (9) yields the following result:

$$[M] + [B] = 2 \frac{q_D}{V_{soma}} a_{21} t . \tag{10}$$

The increase in $[M]+[B]$ over time is attributed to the continuous conversion of dimers into monomers.

Examining the numerical solution of Eqs. (4)-(6) reveals that $[M] \to 0$ as $t \to \infty$. Substituting this into Eq. (10) reveals that the concentration of TDP-43 aggregates can be approximated by the following equation:

$$[B] = 2 \frac{q_D}{V_{soma}} a_{21} t . \tag{11}$$

Substituting Eq. (11) into Eq. (6) results in:

$$[M] = \frac{2 \frac{q_D}{V_{soma}} a_{21}}{k_1 + k_2 2 \frac{q_D}{V_{soma}} a_{21} t} . \tag{12}$$

The approximate solution is provided by Eqs. (8), (11), and (12). It is important to recognize the utility of these equations over extended durations. However, they become invalid when $t \to 0$; for instance, Eq. (12) yields $[M] = \frac{2}{k_1} \frac{q_D}{V_{soma}} a_{21}$, contradicting the initial condition given by Eq. (7b).

2.3. Estimation of the size of the inclusion body

The calculation of the inclusion body growth (see Fig. 1) is conducted as follows. The number of TDP-43 monomers incorporated into a single inclusion body at any given time t is determined according to the following equation [28]:

$$N_{single}(t) = \frac{1}{N_{IB}} \frac{[B](t)}{a_{21}} V_{soma} N_A . \tag{13}$$

Here, N_{IB} represents the number of inclusion bodies in the soma, with the assumption that all inclusion bodies have equal volumes.

Alternatively, $N_{single}(t)$ can be calculated as follows [28]:

$$N_{single}(t) = \frac{V_{single}(t)\rho_{IB}}{MW} N_A , \tag{14}$$

where MW denotes the molecular weight of TDP-43 monomers, which is the sum of the weights of all the atoms within the monomer.

By equating the expressions on the right-hand sides of Eqs. (13) and (14) and solving for the volume of a single inclusion body, the following result is obtained:

$$V_{single}(t) = \frac{[B](t)}{a_{21} N_{IB}} V_{soma} \frac{MW}{\rho_{IB}} . \tag{15}$$

Substituting Eq. (11) into Eq. (15) yields:

$$V_{single}(t) = \frac{2}{N_{IB}} \frac{MW}{\rho_{IB}} q_D t . \tag{16}$$

This implies that the volume of a single inclusion body in the soma increases linearly with both the rate of TDP-43 dimer generation and time.

TDP-43 inclusions within the soma can take on various shapes, ranging from skein-like to rounded [24]. The assumption was made that all inclusion bodies are spherical and of the same size. The volume of a spherical inclusion body can be calculated as follows:

$$V_{single}(t) = \frac{4}{3} \pi r_{IB}^3 (t) . \tag{17}$$

If the right-hand sides of Eqs. (15) and (17) are set equal to each other, and the resulting equation is solved for the radius of the inclusion body, the following result is obtained:

$$r_{IB} = \left(\frac{3}{4\pi} \frac{[B]}{a_{21} N_{IB}} V_{soma} \frac{MW}{\rho_{IB}} \right)^{1/3} . \tag{18}$$

Substituting the approximate solution (11) into Eq. (18) results in:

$$r_{IB} = \left(\frac{3}{2\pi} \frac{q_D}{N_{IB}} \frac{MW}{\rho_{IB}} \right)^{1/3} t^{1/3} . \tag{19}$$

Eq. (19) can be utilized to estimate the rate at which TDP-43 dimers are generated in the soma. If, after the growth period $t_{IB,f}$ the inclusion body's radius attains the size $r_{IB,f}$, then, according to Eq. (19), q_D can be determined as:

$$q_D = \frac{2\pi}{3} \frac{\rho_{IB}}{MW} \frac{N_{IB}}{t_{IB,f}} r_{IB,f}^3 . \tag{20}$$

2.4. Sensitivity of the inclusion body's radius to model parameters

The study investigated the sensitivity of the inclusion body's radius, denoted as r_{IB}, to various parameters in Eq. (19). Local sensitivity coefficients [29-32] were computed, representing the first-order partial derivatives of the observable (in this case, the inclusion body's radius) with respect to, for example, the rate of TDP-43 dimer production, q_D, denoted as $\frac{\partial r_{IB}}{\partial q_D}$. The dimensionless relative sensitivity coefficients [30,33] were determined as the ratio of the relative change in the inclusion body's radius, $\Delta r_{IB} / r_{IB}$, to the relative change in the respective parameter, in this case, $\Delta q_D / q_D$:

$$S_{q_D}^{r_{IB}} = \frac{q_D}{r_{IB}} \frac{\partial r_{IB}}{\partial q_D} = \frac{1}{3} . \tag{21}$$

Eq. (19) was employed to calculate the derivative in Eq. (21). Importantly, the result in Eq. (21) is time-independent, indicating that the sensitivity remains constant at any given time. The positive sign of $S_{q_D}^{r_{IB}}$ suggests that r_{IB} increases with an increase in q_D. Similarly,

$$S_{MW}^{r_{IB}} = \frac{MW}{r_{IB}} \frac{\partial r_{IB}}{\partial MW} = \frac{1}{3} , \tag{22}$$

$$S_{N_{IB}}^{r_{IB}} = \frac{N_{IB}}{r_{IB}} \frac{\partial r_{IB}}{\partial N_{IB}} = -\frac{1}{3}, \tag{23}$$

$$S_{\rho_{IB}}^{r_{IB}} = \frac{\rho_{IB}}{r_{IB}} \frac{\partial r_{IB}}{\partial \rho_{IB}} = -\frac{1}{3}. \tag{24}$$

At large times, the sensitivity of r_{IB} to the kinetic constants k_1, k_2, and k_M derived from the approximate analytical solution (19) is zero. Since the approximate analytical solution is only applicable for large times, I employed the numerical solution to calculate the sensitivity of r_{IB} to the kinetic constants at smaller times. For instance:

$$S_{k_1}^{r_{IB}} = \frac{k_1}{r_{IB}} \frac{\partial r_{IB}}{\partial k_1} \approx \frac{k_1}{r_{IB}} \frac{r_{IB}\left(k_1 + \Delta k_1\right) - r_{IB}\left(k_1\right)}{\Delta k_1}\Bigg|_{\text{other parmeters kept constant}}. \tag{25}$$

Here, $\Delta k_1 = 10^{-3} k_1$ represents the step size. The computations were carried out using various step sizes to assess whether the sensitivity coefficients remained unaffected by changes in the step size.

2.5. Numerical solution

Eqs. (4)-(6) with initial conditions (7) were solved using MATLAB's ODE45 solver (MATLAB R2020b, MathWorks, Natick, MA, USA). To guarantee solution accuracy, the error tolerance parameters, RelTol and AbsTol, were set to 1e-10.

3. Results

Figs. 2-7 display the radius of a TDP-43 inclusion body in a scenario where the soma contains two inclusion bodies of equal size. The model predicts the concentration of TDP-43 aggregates, which are then deposited into the inclusion bodies, leading to their growth. To simplify interpretation, both inclusion bodies are assumed to be spherical, allowing the total volume of TDP-43 aggregates to be recalculated into radii for two identical spherical inclusion bodies.

Among all the model parameters listed in Table 2, I had the least certainty regarding the values of the kinetic constants k_1, k_2, and k_M. Consequently, I conducted an investigation to evaluate the consistency of the model predictions, specifically examining the direct proportionality of the TDP-43 inclusion body radius to the cube root of time, as indicated in Eq. (19), when varying the values of the kinetic constants over a wide range.

Figs. 2-4 are calculated for the scenario of dysfunctional protein degradation machinery $T_{1/2,D} \to \infty$, $T_{1/2,M} \to \infty$, and $T_{1/2,B} \to \infty$. Fig. 2 shows that for $t > 0.04$ year the inclusion body's radius, r_{IB}, remains unaffected by the kinetic constant k_1 governing the conversion of TDP-43 monomers into a misfolded, aggregating form by nucleation. This is consistent with the approximate solution given by Eq. (19), indicating that the radius is insensitive to the kinetic constants. However, the validity of the approximate solution is limited to extended timeframes ($t > 0.04$ year). Fig. 2 shows that numerical solutions for $t > 0.04$ precisely agree with the approximate solution given by Eq. (19), indicating that the inclusion body's radius grows directly in proportion to $t^{1/3}$.

The concentrations of TDP-43 dimers, monomers, and aggregates are plotted in the Supplemental Materials. The concentration of dimers, [*D*], quickly stabilizes (in less than 0.002 years) at a constant value, determined by the balance of dimer production and dimer conversion into monomers (Fig. S1).

As monomers convert into aggregates, the concentration of monomers, [*M*], decreases over time, initially rapidly and then gradually (Fig. S2). The numerical and analytical solutions converge at large times, but the time it takes for the solutions to align depends on the value of k_1. The convergence is slower for larger values of k_1, taking approximately one year for the numerical solution to match the approximate solution when $k_1 = 10^{-4}$ s^{-1}.

The approximate solution indicates a linear increase in the concentration of aggregates over time, with numerical and analytical solutions converging in approximately 0.04 hours (Fig. S3). It is crucial to note that the plotted TDP-43 aggregate concentration does not account for the removal of aggregates from the cytosol due to deposition into inclusion bodies. The model assumes integration of all aggregates into the inclusion bodies.

For various values of k_2, describing the rate of autocatalytic aggregation of TDP-43 monomers, the numerical solution for the inclusion body's radius, r_{IB}, also converges to the approximate solution given Eq. (19). The convergence rate depends on k_2, with the slowest convergence observed for the smallest tested value, $k_2 = 10^{-8}$ μM^{-1} s^{-1}. In this case, it takes approximately 0.4 years for the numerical solution to converge to the approximate solution (Fig. 3). The concentrations of TDP-43 dimers, monomers, and aggregates also quickly converge to those given by the approximate solution (Figs. S4-S6). Notably, the concentration of aggregates reaches a linearly increasing curve with time (Fig. S6), attributed to the constant supply of TDP-43 dimers at a rate of q_D.

Testing the numerical solution for various values of k_M, representing the rate of conversion of TDP-43 dimers into monomers, revealed that the numerical solution for r_{IB} converges to the cube root of time dependence, as predicted by the approximate solution in Eq. (19). The rate of convergence depends on the value of k_M (see Fig. 4), with the slowest convergence observed for the smallest tested value of 10^{-6} s^{-1}. The concentration of TDP-43 dimers, [*D*] (Fig. S7), is influenced by k_M, as it is inversely proportional to k_M for a constant value of q_D (see Eq. (8)). Numerical solutions converge to the approximate analytical solutions predicted by Eq. (8), resulting in three distinct curves corresponding to different values of k_M (Fig. S7). Conversely, the concentrations of monomers, [*M*], and aggregates, [*B*], converge to the same analytical solution independent of the value of k_M (Figs. S8 and S9).

Figs. 5-7 are computed for physiologically relevant half-lives of TDP-43 dimers, monomers, and aggregates ($T_{1/2,D} = 4.32\times10^4$ s, $T_{1/2,M} = 4.32\times10^4$ s, and $T_{1/2,B} = 1.30\times10^5$ s). The approximate solution is not included as it is exclusively applicable to the scenario involving infinite half-lives of TDP-43 dimers, monomers, and aggregates. In contrast to the situation with infinite half-lives, the curves depicting the radii of inclusion bodies do not converge to the curve displaying a cube root of time as time increases. For different values of kinetic constants (k_1, k_2, and k_M), the curves representing r_{IB} converge to different constant values determined by the production of TDP-43 aggregates and their degradation due to their finite half-life.

The concentration of TDP-43 dimers, [*D*], is independent of kinetic constants k_1 and k_2 (Figs. S10 and S13), but depends on the value of k_M (Fig. S16). The concentration of TDP-43 monomers, [*M*], depends on the values of k_1, k_2, and k_M (Figs. S11, S14, and S17). The concentration of TDP-43 aggregates, [*B*], depends on the values of k_1, k_2, and k_M (Figs. S12, S15, and S18).

Fig. 8 explores the sensitivity of the inclusion body's radius, r_{IB}, to the kinetic constants k_1, k_2, and k_M for the scenario with infinite half-life of TDP-43 dimers, monomers, and aggregates. The sensitivity is positive at small times and, at large times, it converges toward the limiting value of zero, consistent with the approximate analytical solution (19).

4. Discussion, limitations of the model, and future directions

This paper has formulated a model for the growth of TDP-43 inclusion bodies. The model predicts the concentrations of TDP-43 dimers, monomers, and aggregates. The model operates under the assumption that all aggregates integrate into the inclusion bodies.

In the case of dysfunctional protein degradation machinery, leading to infinite half-lives of protein dimers, monomers, and aggregates, the model predicts that the inclusion body's radius increases in proportion to the cube root of time. As kinetic constants governing the rates of TDP-43 monomerization, nucleation, and autocatalytic growth are not documented in the literature, an investigation was conducted to determine the consistency of model predictions across a wide range of values for these kinetic constants. The findings revealed that model predictions are influenced by the kinetic constants only at small times. The derived approximate solution, valid for large times, demonstrates that the concentrations of TDP-43 monomers and aggregates and the radius of the inclusion body remain unaffected by the kinetic constants. The approximate solution indicates a linear increase in aggregate concentration over time, attributed to the continuous synthesis of TDP-43 dimers in the cytoplasm.

The approximate solution becomes invalid for the scenario with physiologically relevant half-lives of TDP-43 dimers, monomers, and aggregates. Unlike the situation with infinite half-lives, the curves depicting the radii of inclusion bodies do not converge to the curve displaying a cube root of time as time increases. For various values of kinetic constants, the curves representing concentrations of monomers and aggregates, as well as the curves depicting the inclusion body radii, converge to distinct constant values.

For infinite half-lives of TDP-43 dimers, monomers, and aggregates the sensitivity of the inclusion body's radius to the kinetic constants is positive at small times and, at large times, it converges toward the limiting value of zero. This indicates that at large times, the inclusion body's radius becomes independent of the kinetic constants.

The analysis presented here has limitations, primarily due to its reliance on a simplified mechanism of TDP-43 cytoplasmic mislocalization and subsequent aggregation, compounded by the absence of precise values for kinetic constants.

Future studies should concentrate on developing more precise models for TDP-43 oligomerization, covering the entire spectrum of oligomeric species, including trimers, tetramers, and multimers. Furthermore, there is a need to integrate the processes of TDP-43 phosphorylation and ubiquitination into these models. Investigating the potential prion-like spread of pathological TDP-43 species is also a crucial avenue for future exploration.

Acknowledgment

AVK acknowledges the support provided by the National Science Foundation (grant CBET-2042834) and the Alexander von Humboldt Foundation through the Humboldt Research Award.

References

1. Ishii T, Kawakami E, Endo K, Misawa H, Watabe K. 2017 Formation and spreading of TDP-43 aggregates in cultured neuronal and glial cells demonstrated by time-lapse imaging. *PLoS One* **12,** e0179375. (doi:10.1371/journal.pone.0179375)

2. Jo M, Lee S, Jeon Y, Kim S, Kwon Y, Kim H. 2020 The role of TDP-43 propagation in neurodegenerative diseases: Integrating insights from clinical and experimental studies. *Exp. Mol. Med.* **52,** 1652-1662. (doi:10.1038/s12276-020-00513-7)

3. Prasad A, Bharathi V, Sivalingam V, Girdhar A, Patel BK. 2019 Molecular mechanisms of TDP-43 misfolding and pathology in amyotrophic lateral sclerosis. *Frontiers in Molecular Neuroscience* **12,** (doi:10.3389/fnmol.2019.00025)

4. Capitini C, Conti S, Perni M, Guidi F, Cascella R, De Poli A, Penco A, Relini A, Cecchi C, Chiti F. 2014 TDP-43 inclusion bodies formed in bacteria are structurally amorphous, non-amyloid and inherently toxic to neuroblastoma cells. *PLoS One* **9,** e86720. (doi:10.1371/journal.pone.0086720)

5. Oiwa K, Watanabe S, Onodera K, Iguchi Y, Kinoshita Y, Komine O, Sobue A, Okada Y, Katsuno M, Yamanaka K. 2023 Monomerization of TDP-43 is a key determinant for inducing TDP-43 pathology in amyotrophic lateral sclerosis. *Sci. Adv.* **9,** eadf6895. (doi:10.1126/sciadv.adf6895)

6. Sugai A, Kato T, Koyama A, Koike Y, Kasahara S, Konno T, Ishihara T, Onodera O. 2018 Robustness and vulnerability of the autoregulatory system that maintains nuclear TDP-43 levels: A trade-off hypothesis for ALS pathology based on in silico data. *Front. Neurosci.* **12,** 28. (doi:10.3389/fnins.2018.00028)

7. Sun Y, Medina Cruz A, Hadley KC, Galant NJ, Law R, Vernon RM, Morris VK, Robertson J, Chakrabartty A. 2019 Physiologically important electrolytes as regulators of TDP-43 aggregation and droplet-phase behavior. *Biochemistry (N. Y.)* **58,** 590-607. (doi:10.1021/acs.biochem.8b00842)

8. French RL, Grese ZR, Aligireddy H, Dhavale DD, Reeb AN, Kedia N, Kotzbauer PT, Bieschke J, Ayala YM. 2019 Detection of TAR DNA-binding protein 43 (TDP-43) oligomers as initial intermediate species during aggregate formation. *J. Biol. Chem.* **294,** 6696-6709. (doi:10.1074/jbc.RA118.005889)

9. Suk TR, Rousseaux MWC. 2020 The role of TDP-43 mislocalization in amyotrophic lateral sclerosis. *Mol. Neurodegener* **15,** 45-1. (doi:10.1186/s13024-020-00397-1)

10. Pérez-Berlanga M, Wiersma VI, Zbinden A, De Vos L, Wagner U, Foglieni C, Mallona I, Betz KM, Cléry A, Weber J, Guo Z, Rigort R, de Rossi P, Manglunia R, Tantardini E, Sahadevan S, Stach O, Hruska-Plochan M, Allain FH, Paganetti P, Polymenidou M. 2023 Loss of TDP-43 oligomerization or RNA binding elicits distinct aggregation patterns. *EMBO J.* **42,** e111719. (doi:10.15252/embj.2022111719)

11. Necarsulmer J, Simon J, Evangelista B, Chen Y, Tian X, Nafees S, Marquez Gonzalez A, Jiang H, Wang P, Ajit D, Nikolova V, Harper K, Ezzell J, Feng-Chang, Beltran A, Moy S, Cohen T. 2023

RNA-binding deficient TDP-43 drives cognitive decline in a mouse model of TDP-43 proteinopathy. eLife Sciences Publications, Ltd.

12. Meneses A, Koga S, O'Leary J, Dickson DW, Bu G, Zhao N. 2021 TDP-43 pathology in Alzheimer's disease. *Molecular Neurodegeneration* **16,** 84. (doi:10.1186/s13024-021-00503-x)

13. Chhangani D, Martín-Peña A, Rincon-Limas DE. 2021 Molecular, functional, and pathological aspects of TDP-43 fragmentation. *iScience* **24,** 102459. (doi:10.1016/j.isci.2021.102459)

14. Glass JD. 2020 Stathmin-2: Adding another piece to the puzzle of TDP-43 proteinopathies and neurodegeneration. *J. Clin. Invest.* **130,** 5677-5680. (doi:10.1172/JCI142854)

15. Jiang L, Xue W, Hong J, Zhang J, Li M, Yu S, He J, Hu H. 2017 The N-terminal dimerization is required for TDP-43 splicing activity. *Scientific Reports* **7,** 6196. (doi:10.1038/s41598-017-06263-3)

16. Sun Y, Arslan PE, Won A, Yip CM, Chakrabartty A. 2014 Binding of TDP-43 to the 3′UTR of its cognate mRNA enhances its solubility. *Biochemistry (N. Y.)* **53,** 5885-5894. (doi:10.1021/bi500617x)

17. Chong PA, Forman-Kay J. 2016 A new phase in ALS research. *Structure* **24,** 1435-1436. (doi:10.1016/j.str.2016.08.003)

18. Kuznetsov AV. 2023 Numerical and analytical simulation of the growth of amyloid-β plaques. *bioRxiv* 2023.09.11.557187. (doi:10.1101/2023.09.11.557187)

19. Kuznetsov IA, Kuznetsov AV. 2022 An analytical solution simulating growth of Lewy bodies. *Math. Med. Biol.* **39,** 299-312. (doi:10.1093/imammb/dqac006)

20. Kuznetsov AV. 2023 Lewy body radius growth: The hypothesis of the cube root of time dependency. *bioRxiv* 2023.10.30.564787. (doi:10.1101/2023.10.30.564787)

21. Morris AM, Watzky MA, Agar JN, Finke RG. 2008 Fitting neurological protein aggregation kinetic data via a 2-step, minimal/"ockham's razor" model: The finke-watzky mechanism of nucleation followed by autocatalytic surface growth. *Biochemistry* **47,** 2413-2427. (doi:10.1021/bi701899y)

22. Iashchishyn IA, Sulskis D, Nguyen Ngoc M, Smirnovas V, Morozova-Roche LA. 2017 Finke-watzky two-step nucleation-autocatalysis model of S100A9 amyloid formation: Protein misfolding as "nucleation" event. *ACS Chem. Neurosci.* **8,** 2152-2158. (doi:10.1021/acschemneuro.7b00251)

23. Finke RG, Watzky MA, Whitehead CB. 2020 Response to "Particle size is a primary determinant for sigmoidal kinetics of nanoparticle formation: A "Disproof" of the Finke–Watzky (F-W) nanoparticle nucleation and growth mechanism". *Chem. Mater.* **32,** 3657-3672. (doi:10.1021/acs.chemmater.0c00780)

24. Cascella R, Bigi A, Riffert DG, Gagliani MC, Ermini E, Moretti M, Cortese K, Cecchi C, Chiti F. 2022 A quantitative biology approach correlates neuronal toxicity with the largest inclusions of TDP-43. *Science Advances* **8,** eabm6376. (doi:10.1126/sciadv.abm6376)

25. Hadley KC, Rakhit R, Guo H, Sun Y, Jonkman JEN, McLaurin J, Hazrati L, Emili A, Chakrabartty A. 2015 Determining composition of micron-scale protein deposits in neurodegenerative disease by spatially targeted optical microproteomics. *eLife* **4,** e09579. (doi:10.7554/eLife.09579)

26. Ling S, Albuquerque CP, Han JS, Lagier-Tourenne C, Tokunaga S, Zhou H, Cleveland DW. 2010 ALS-associated mutations in TDP-43 increase its stability and promote TDP-43 complexes with FUS/TLS. *Proc. Natl. Acad. Sci. U. S. A.* **107,** 13318-13323. (doi:10.1073/pnas.1008227107)

27. Cavicchi RE, King J, Ripple DC. 2018 Measurement of average aggregate density by sedimentation and brownian motion analysis. *J. Pharm. Sci.* **107,** 1304-1312. (doi:10.1016/j.xphs.2018.01.013)

28. Watzky MA, Finney EE, Finke RG. 2008 Transition-metal nanocluster size vs formation time and the catalytically effective nucleus number: A mechanism-based treatment. *J. Am. Chem. Soc.* **130,** 11959-11969. (doi:10.1021/ja8017412)

29. Beck JV, Arnold KJ. 1977 *Parameter Estimation in Science and Engineering.* New York: Wiley.

30. Zadeh KS, Montas HJ. 2010 A class of exact solutions for biomacromolecule diffusion-reaction in live cells. *J. Theor. Biol.* **264,** 914-933. (doi:10.1016/j.jtbi.2010.03.028)

31. Zi Z. 2011 Sensitivity analysis approaches applied to systems biology models. *Iet Systems Biology* **5,** 336-346. (doi:10.1049/iet-syb.2011.0015)

32. Kuznetsov IA, Kuznetsov AV. 2019 Investigating sensitivity coefficients characterizing the response of a model of tau protein transport in an axon to model parameters. *Comput. Methods Biomech. Biomed. Engin.* **22,** 71-83. (doi:10.1080/10255842.2018.1534233)

33. Kacser H, Burns JA, Fell DA. 1995 The control of flux. *Biochem. Soc. Trans.* **23,** 341-366. (doi:10.1042/bst0230341)

34. Bieschke J, Zhang Q, Powers ET, Lerner RA, Kelly JW. 2005 Oxidative metabolites accelerate Alzheimer's amyloidogenesis by a two-step mechanism, eliminating the requirement for nucleation. *Biochemistry* **44,** 4977-4983. (doi:10.1021/bi0501030)

35. Vestergaard M, Kerman K, Saito M, Nagatani N, Takamura Y, Tamiya E. 2005 A rapid label-free electrochemical detection and kinetic study of Alzheimer's amyloid beta aggregation. *J. Am. Chem. Soc.* **127,** 11892-11893. (doi:10.1021/ja052522q)

36. Lu K, Jacob J, Thiyagarajan P, Conticello VP, Lynn DG. 2003 Exploiting amyloid fibril lamination for nanotube self-assembly. *J. Am. Chem. Soc.* **125,** 6391-6393. (doi:10.1021/ja0341642)

37. Dong J, Shokes JE, Scott RA, Lynn DG. 2006 Modulating amyloid self-assembly and fibril morphology with zn(II). *J. Am. Chem. Soc.* **128,** 3540-3542. (doi:10.1021/ja055973j)

38. Zirah S, Kozin SA, Mazur AK, Blond A, Cheminant M, Ségalas-Milazzo I, Debey P, Rebuffat S. 2006 Structural changes of region 1-16 of the Alzheimer disease amyloid beta-peptide upon zinc binding and in vitro aging. *J. Biol. Chem.* **281,** 2151-2161. (doi:10.1074/jbc.M504454200)

39. Fink AL. 2006 The aggregation and fibrillation of alpha-synuclein. *Acc. Chem. Res.* **39,** 628-634. (doi:10.1021/ar050073t)

40. Sode K, Usuzaka E, Kobayashi N, Ochiai S. 2005 Engineered alpha-synuclein prevents wild type and familial parkin variant fibril formation. *Biochem. Biophys. Res. Commun.* **335,** 432-436. (doi:10.1016/j.bbrc.2005.07.100)

41. Chen S, Ferrone FA, Wetzel R. 2002 Huntington's disease age-of-onset linked to polyglutamine aggregation nucleation. *Proc. Natl. Acad. Sci. U. S. A.* **99,** 11884-11889. (doi:10.1073/pnas.182276099)

42. Wetzel R. 2006 Kinetics and thermodynamics of amyloid fibril assembly. *Acc. Chem. Res.* **39,** 671-679. (doi:10.1021/ar050069h)

43. Ban T, Yamaguchi K, Goto Y. 2006 Direct observation of amyloid fibril growth, propagation, and adaptation. *Acc. Chem. Res.* **39,** 663-670. (doi:10.1021/ar050074l)

44. Dumoulin M, Kumita JR, Dobson CM. 2006 Normal and aberrant biological self-assembly: Insights from studies of human lysozyme and its amyloidogenic variants. *Acc. Chem. Res.* **39,** 603-610. (doi:10.1021/ar050070g)

Figure captions

Fig. 1. A diagram depicting a neuron with two TDP-43 inclusion bodies of equal size located in the soma. *Figure generated with the aid of servier medical art, licensed under a creative commons attribution 3.0 generic license. http://Smart.servier.com.*

Fig. 2. (a) The radius of the growing inclusion body vs time (in years). The model predicts the total volume of all inclusion bodies in the soma as $N_{IB}V_{single}$. Assuming that all inclusion bodies have the same volume, the total volume is then recalculated into the volume of a single inclusion body, denoted as V_{single} (Eqs. (15) and (16)). The predicted volume is then converted into the radius of a sphere with an equivalent volume to facilitate interpretation. (b) Similar to Fig. 2a, but concentrating on a specific time range of [0 0.04 year]. The concentration of the misfolded form of TDP-43, [*B*], is obtained by numerically solving Eqs. (4)-(6) with the initial condition (7), and then the radius of the inclusion body is calculated by using Eq. (18). The approximate solution is determined by employing Eq. (19). The presented scenario assumes dysfunctional protein degradation machinery with $T_{1/2,D} \to \infty$, $T_{1/2,M} \to \infty$, and $T_{1/2,B} \to \infty$. The results are displayed for three values of k_1. $k_2 = 10^{-6}$ μM^{-1} s^{-1} and $k_M = 10^{-4}$ s^{-1}.

Fig. 3. (a) The radius of the growing inclusion body vs time (in years). (b) Similar to Fig. 3a, but concentrating on a specific time range of [0 0.4 year]. The approximate solution is determined by employing Eq. (19). The presented scenario assumes dysfunctional protein degradation machinery with $T_{1/2,D} \to \infty$, $T_{1/2,M} \to \infty$, and $T_{1/2,B} \to \infty$. The results are displayed for three values of k_2. $k_1 = 10^{-6}$ s^{-1} and $k_M = 10^{-4}$ s^{-1}.

Fig. 4. (a) The radius of the growing inclusion body vs time (in years). (b) Similar to Fig. 4a, but concentrating on a specific time range of [0 1 year]. The approximate solution is determined by employing Eq. (19). The presented scenario assumes dysfunctional protein degradation machinery with $T_{1/2,D} \to \infty$, $T_{1/2,M} \to \infty$, and $T_{1/2,B} \to \infty$. The results are displayed for three values of k_M. $k_1 = 10^{-6}$ s^{-1} and $k_2 = 10^{-6}$ μM^{-1} s^{-1}.

Fig. 5. (a) The radius of the growing inclusion body vs time (in years). (b) Similar to Fig. 5a, but concentrating on a specific time range of [0 0.04 year]. The presented scenario assumes physiologically relevant values for the half-lives of TDP-43 dimers, monomers, and aggregates. $T_{1/2,D} = 4.32 \times 10^4$ s, $T_{1/2,M} = 4.32 \times 10^4$ s, and $T_{1/2,B} = 1.30 \times 10^5$ s. The approximate solution is not displayed as it applies

exclusively to the scenario involving infinite half-lives of TDP-43 dimers, monomers, and aggregates. The results are displayed for three values of k_1. $k_2 = 10^{-6}$ μM^{-1} s^{-1} and $k_M = 10^{-4}$ s^{-1}.

Fig. 6. (a) The radius of the growing inclusion body vs time (in years). (b) Similar to Fig. 6a, but concentrating on a specific time range of [0 0.04 year]. The presented scenario assumes physiologically relevant values for the half-lives of TDP-43 dimers, monomers, and aggregates. $T_{1/2,D} = 4.32 \times 10^4$ s, $T_{1/2,M} = 4.32 \times 10^4$ s, and $T_{1/2,B} = 1.30 \times 10^5$ s. The approximate solution is not displayed as it applies exclusively to the scenario involving infinite half-lives of TDP-43 dimers, monomers, and aggregates. The results are displayed for three values of k_2. $k_1 = 10^{-6}$ s^{-1} and $k_M = 10^{-4}$ s^{-1}.

Fig. 7. (a) The radius of the growing inclusion body vs time (in years). (b) Similar to Fig. 7a, but concentrating on a specific time range of [0 0.04 year]. The presented scenario assumes physiologically relevant values for the half-lives of TDP-43 dimers, monomers, and aggregates. $T_{1/2,D} = 4.32 \times 10^4$ s, $T_{1/2,M} = 4.32 \times 10^4$ s, and $T_{1/2,B} = 1.30 \times 10^5$ s. The approximate solution is not displayed as it applies exclusively to the scenario involving infinite half-lives of TDP-43 dimers, monomers, and aggregates. The results are displayed for three values of k_M. $k_1 = 10^{-6}$ s^{-1} and $k_2 = 10^{-6}$ μM^{-1} s^{-1}.

Fig. 8. The dimensionless sensitivity of the inclusion body's radius, r_{IB}, to:

(a) the rate constant linked to the first pseudoelementary step in the F-W model, describing aggregate formation through nucleation, k_1 (calculated for $k_2 = 10^{-6}$ μM^{-1} s^{-1}, $k_M = 10^{-4}$ s^{-1} for three distinct values of k_1);

(b) the rate constant associated with the second pseudoelementary step in the F-W model, describing aggregate formation through autocatalytic growth, k_2 (calculated for $k_1 = 10^{-6}$ s^{-1}, $k_M = 10^{-4}$ s^{-1} for three distinct values of k_2);

(c) the rate constant linked to the reaction describing the conversion of TDP-43 dimers into monomers, k_M (calculated for $k_1 = 10^{-6}$ s^{-1}, $k_2 = 10^{-6}$ μM^{-1} s^{-1} for three distinct values of k_M).

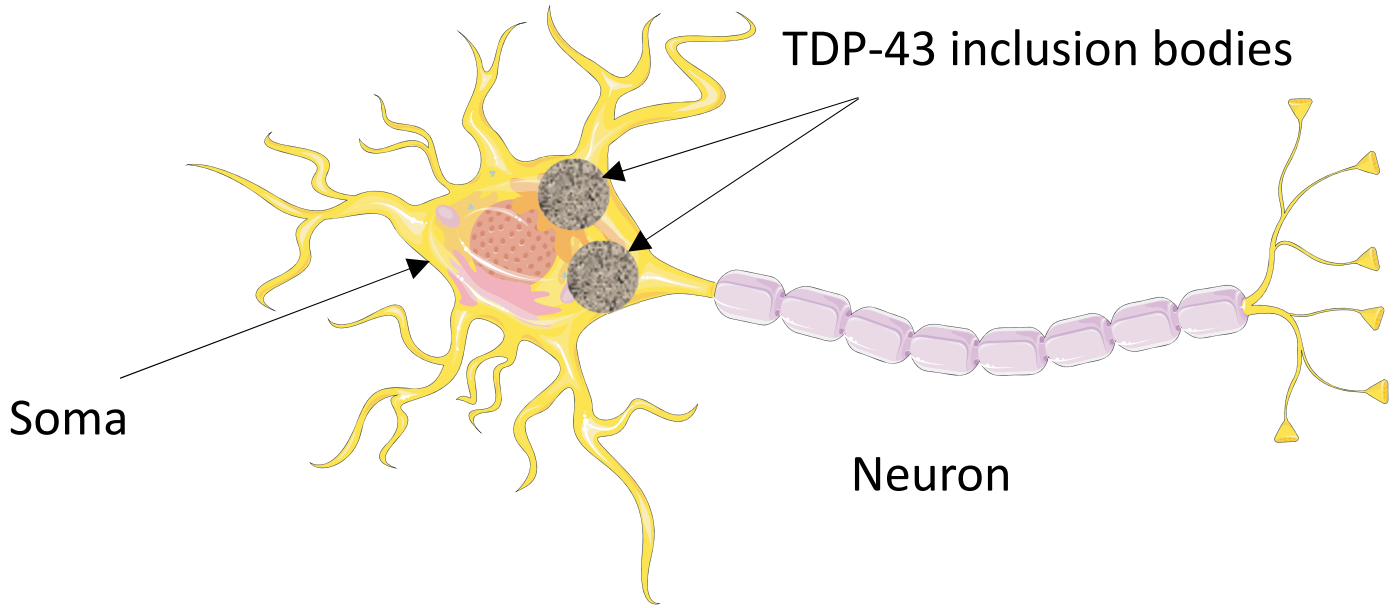

Figure 1

(a)

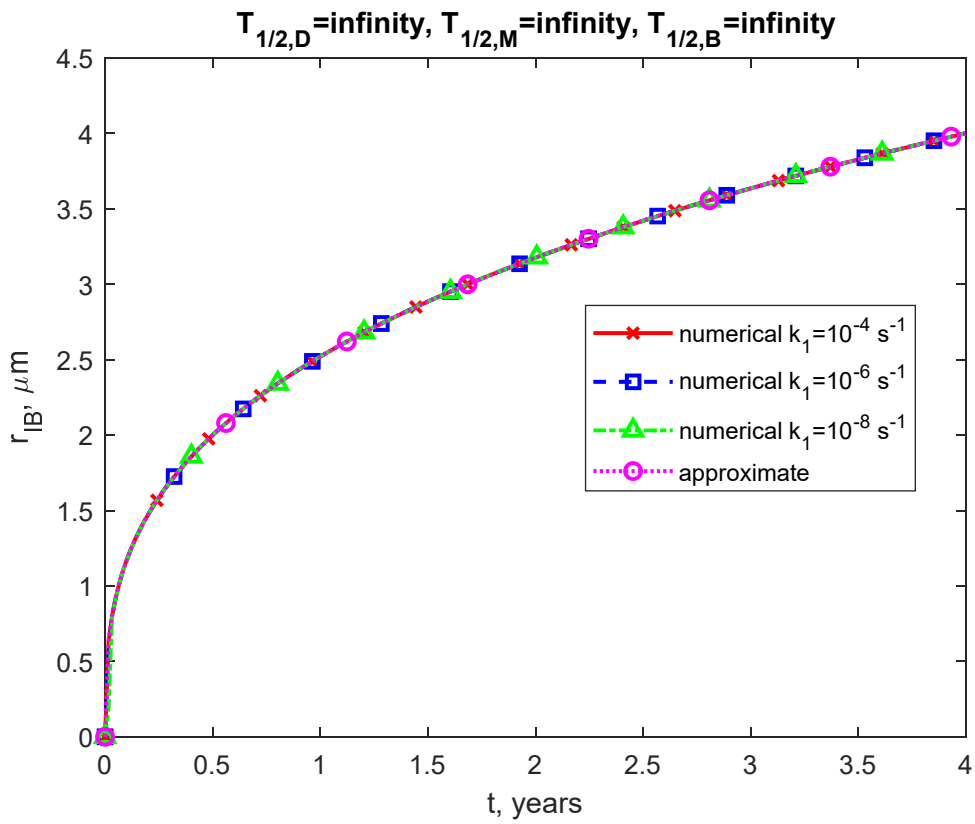
T1/2,D=infinity, T1/2,M=infinity, T1/2,B=infinity
rIB, μm
t, years
numerical k1=10-4 s-1
numerical k1=10-6 s-1
numerical k1=10-8 s-1
approximate

(b)

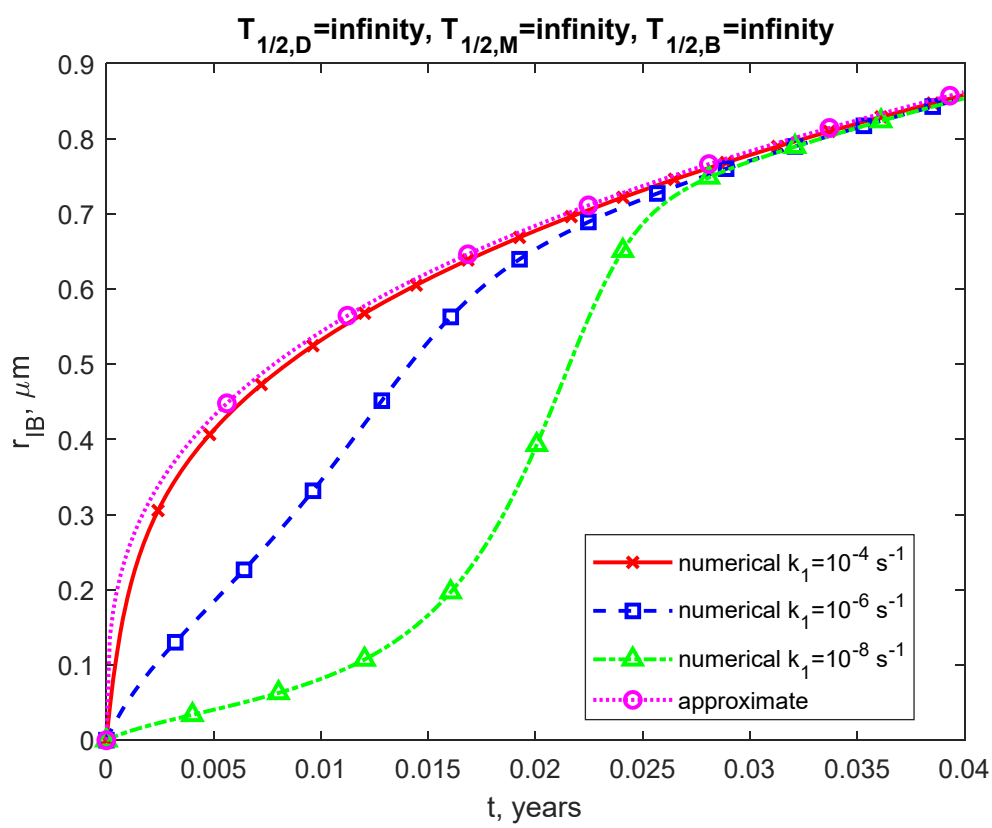
T1/2,D=infinity, T1/2,M=infinity, T1/2,B=infinity
rIB, μm
t, years
numerical k1=10-4 s-1
numerical k1=10-6 s-1
numerical k1=10-8 s-1
approximate

Figure 2

(a)

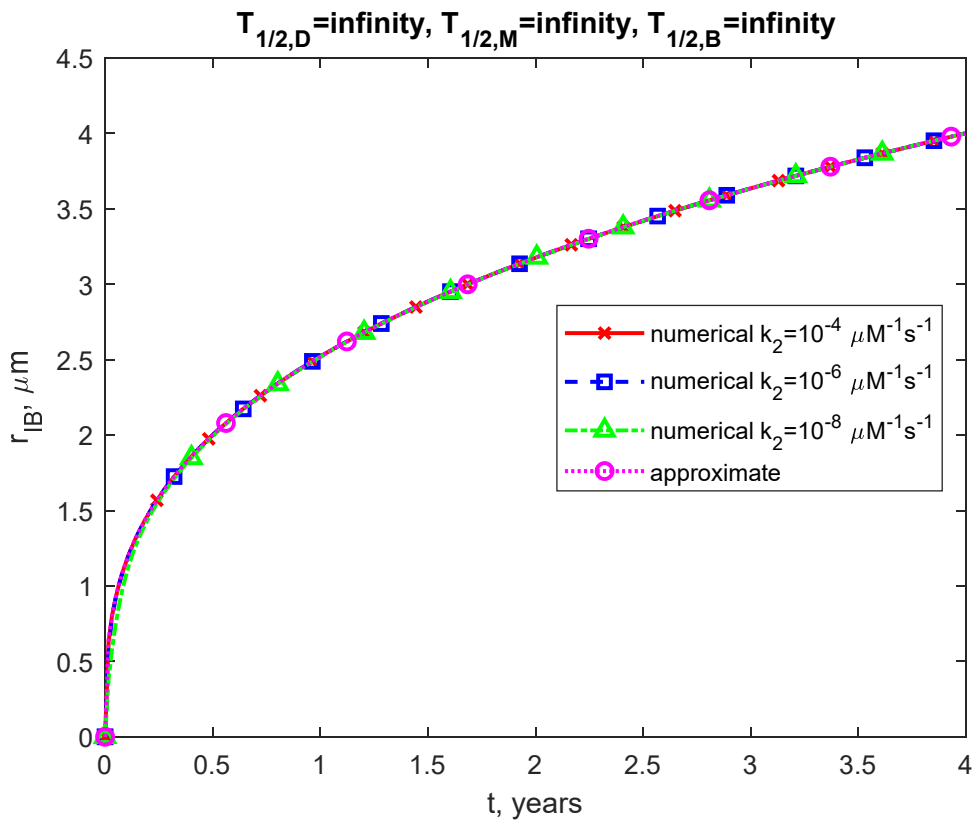
T1/2,D=infinity, T1/2,M=infinity, T1/2,B=infinity
rIB, μm
t, years
numerical k2=10-4 μM-1s-1
numerical k2=10-6 μM-1s-1
numerical k2=10-8 μM-1s-1
approximate

(b)

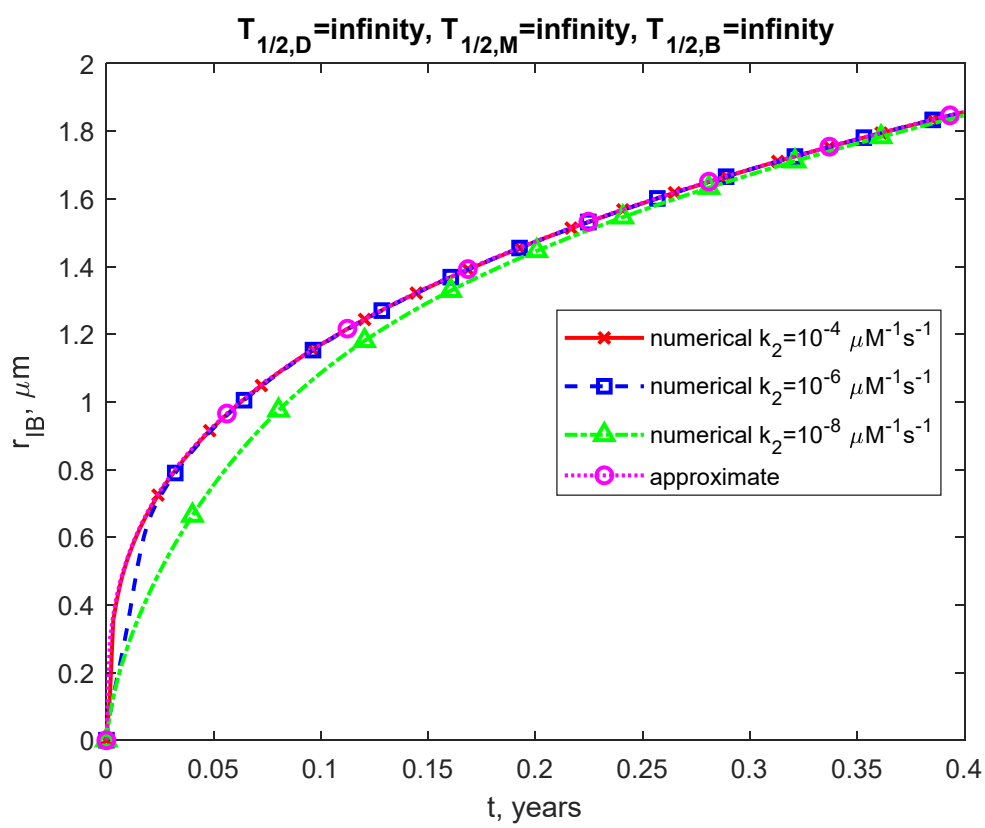
T1/2,D=infinity, T1/2,M=infinity, T1/2,B=infinity
rIB, μm
t, years
numerical k2=10-4 μM-1s-1
numerical k2=10-6 μM-1s-1
numerical k2=10-8 μM-1s-1
approximate

Figure 3

(a)

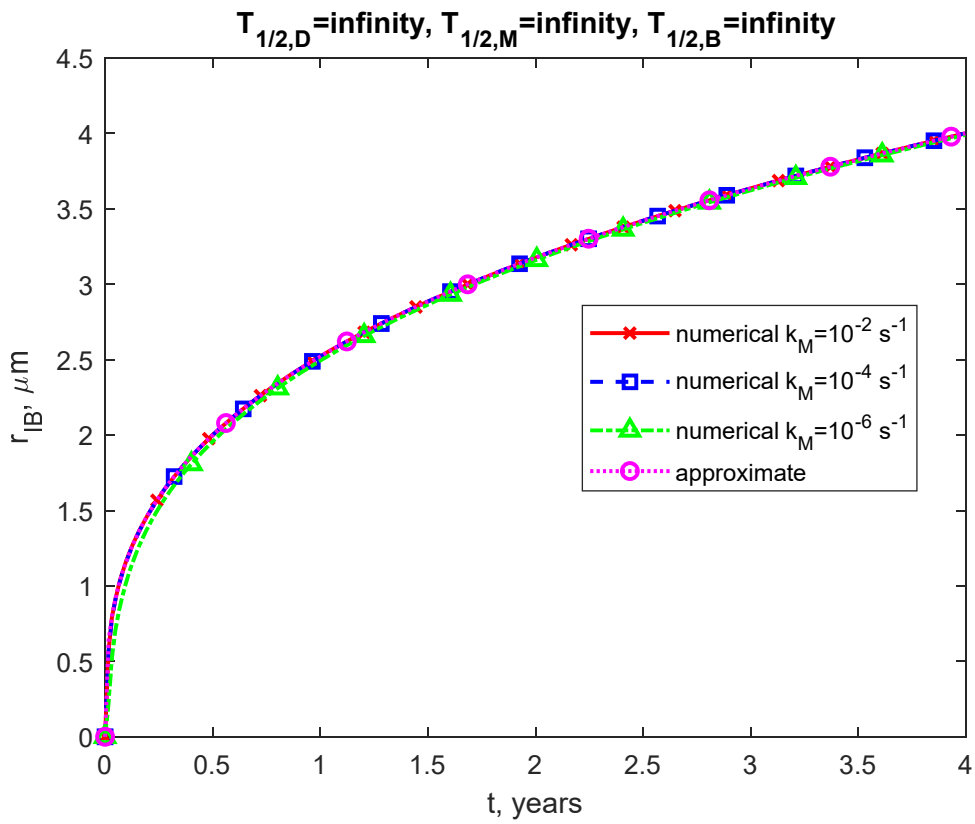
T 1/2,D=infinity, T 1/2,M=infinity, T 1/2,B=infinity
r IB, μm
t, years
numerical k M=10-2 s-1
numerical k M=10-4 s-1
numerical k M=10-6 s-1
approximate

(b)

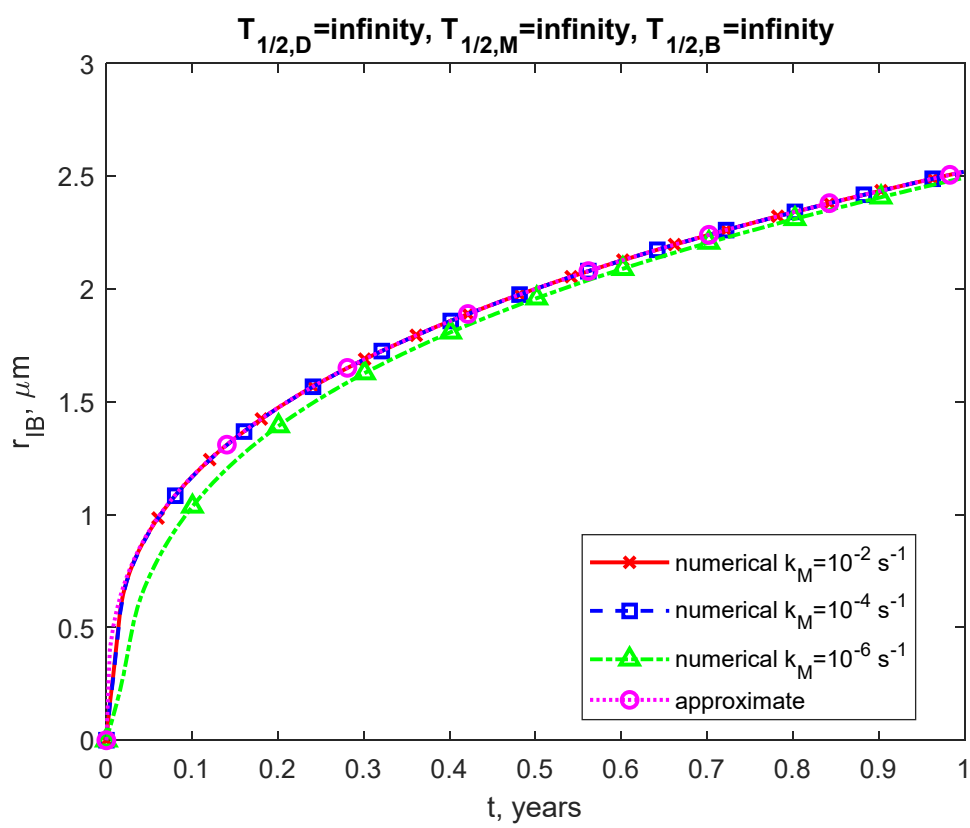
T 1/2,D=infinity, T 1/2,M=infinity, T 1/2,B=infinity
r IB, μm
t, years
numerical k M=10-2 s-1
numerical k M=10-4 s-1
numerical k M=10-6 s-1
approximate

Figure 4

(a)

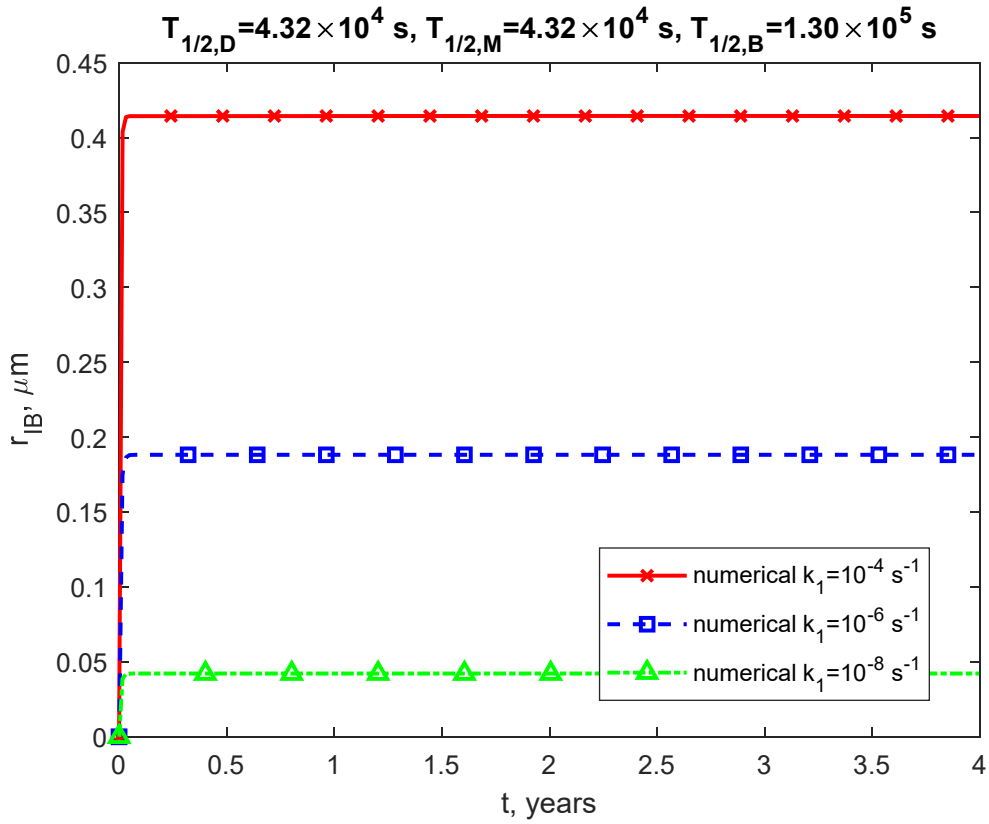
$T_{1/2,D}$=4.32×10^4 s, $T_{1/2,M}$=4.32×10^4 s, $T_{1/2,B}$=1.30×10^5 s
r_{IB}, μm
t, years
numerical k_1=10^-4 s^-1
numerical k_1=10^-6 s^-1
numerical k_1=10^-8 s^-1

(b)

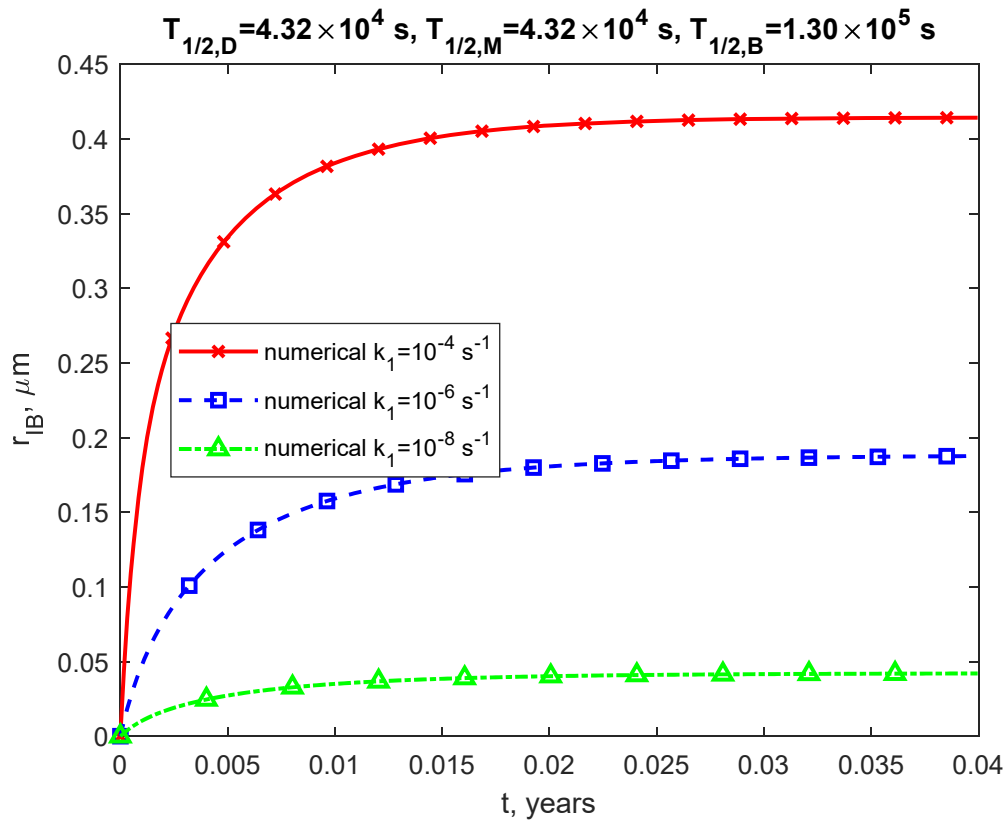
$T_{1/2,D}$=4.32×10^4 s, $T_{1/2,M}$=4.32×10^4 s, $T_{1/2,B}$=1.30×10^5 s
r_{IB}, μm
t, years
numerical k_1=10^-4 s^-1
numerical k_1=10^-6 s^-1
numerical k_1=10^-8 s^-1

Figure 5

(a)

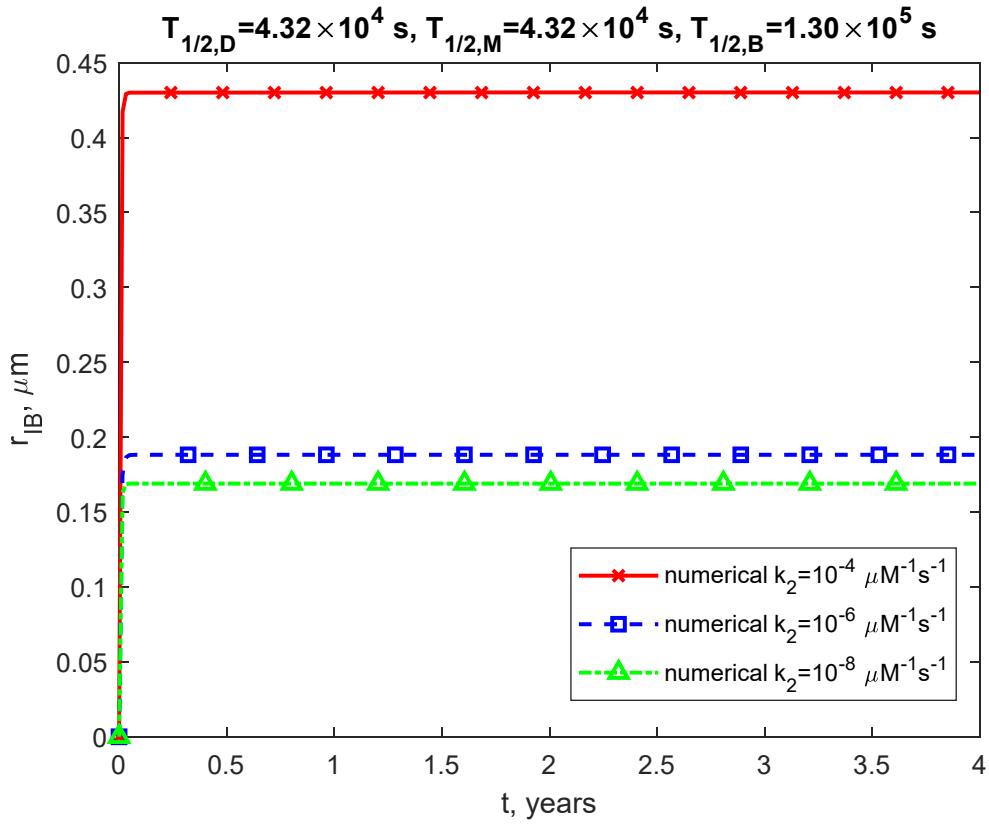
$T_{1/2,D}$=4.32×10^4 s, $T_{1/2,M}$=4.32×10^4 s, $T_{1/2,B}$=1.30×10^5 s
r_{IB}, μm
t, years
numerical k_2=10^-4 μM^-1s^-1
numerical k_2=10^-6 μM^-1s^-1
numerical k_2=10^-8 μM^-1s^-1

(b)

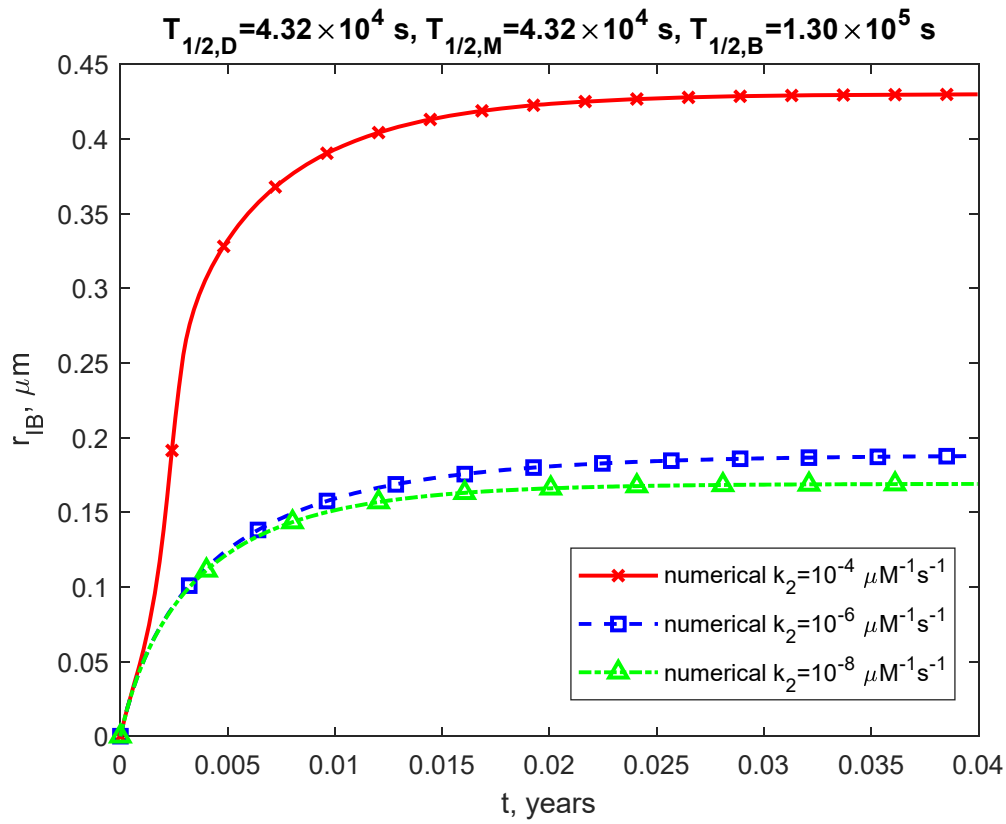
$T_{1/2,D}$=4.32×10^4 s, $T_{1/2,M}$=4.32×10^4 s, $T_{1/2,B}$=1.30×10^5 s
r_{IB}, μm
t, years
numerical k_2=10^-4 μM^-1s^-1
numerical k_2=10^-6 μM^-1s^-1
numerical k_2=10^-8 μM^-1s^-1

Figure 6

(a)

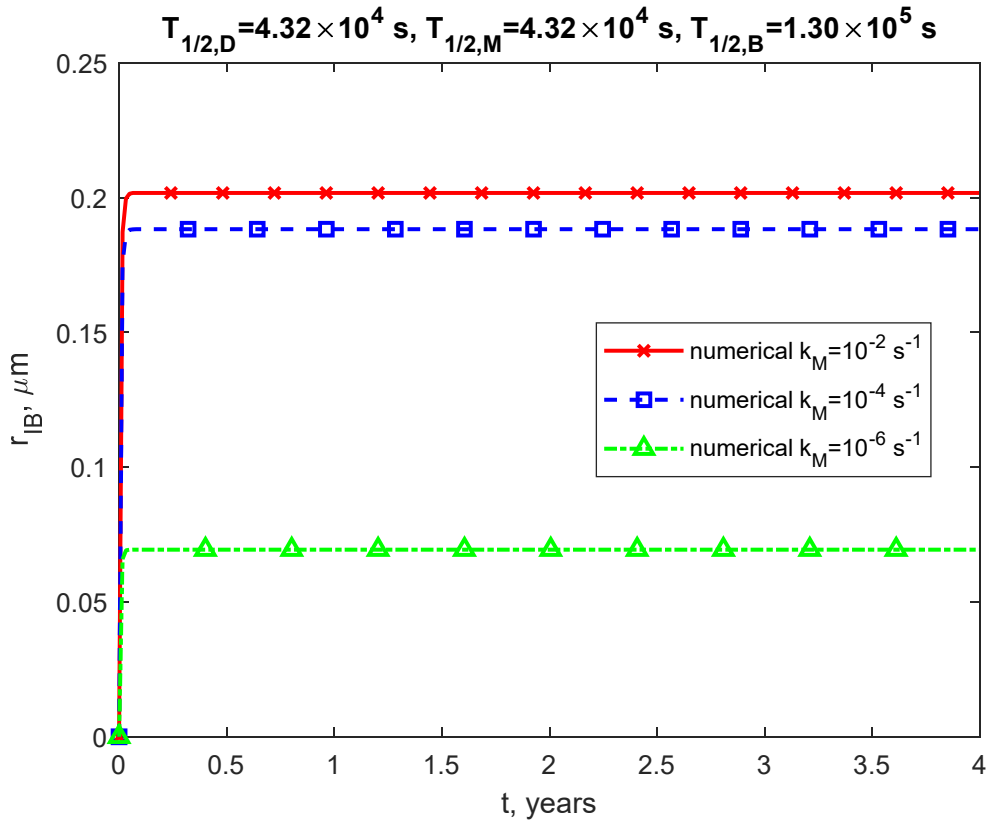
$T_{1/2,D}$=4.32×10^4 s, $T_{1/2,M}$=4.32×10^4 s, $T_{1/2,B}$=1.30×10^5 s
r_{IB}, μm
t, years
numerical k_M=10^-2 s^-1
numerical k_M=10^-4 s^-1
numerical k_M=10^-6 s^-1

(b)

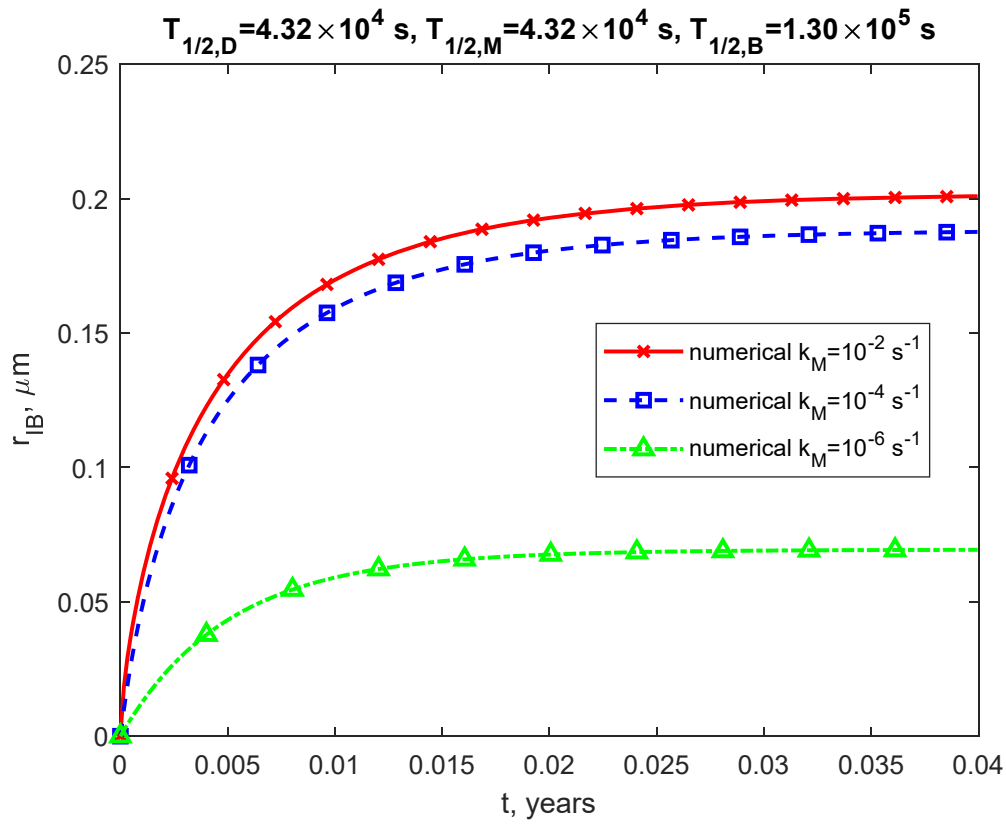
$T_{1/2,D}$=4.32×10^4 s, $T_{1/2,M}$=4.32×10^4 s, $T_{1/2,B}$=1.30×10^5 s
r_{IB}, μm
t, years
numerical k_M=10^-2 s^-1
numerical k_M=10^-4 s^-1
numerical k_M=10^-6 s^-1

Figure 7

(a)

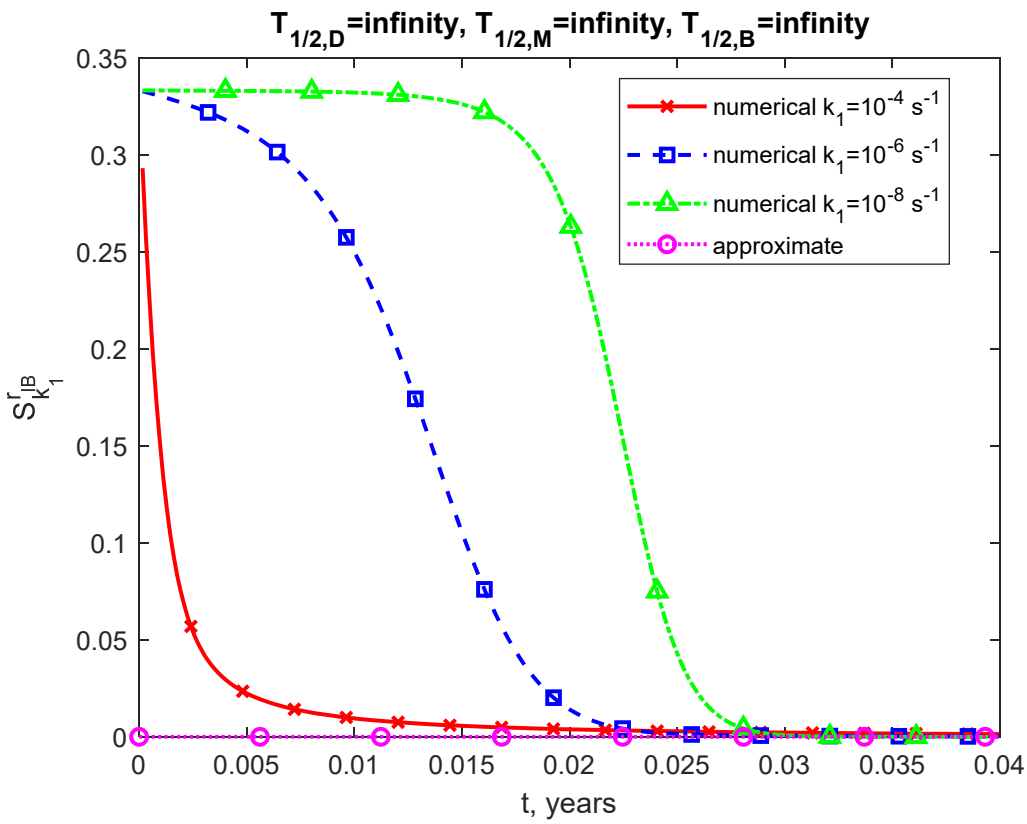

(b)

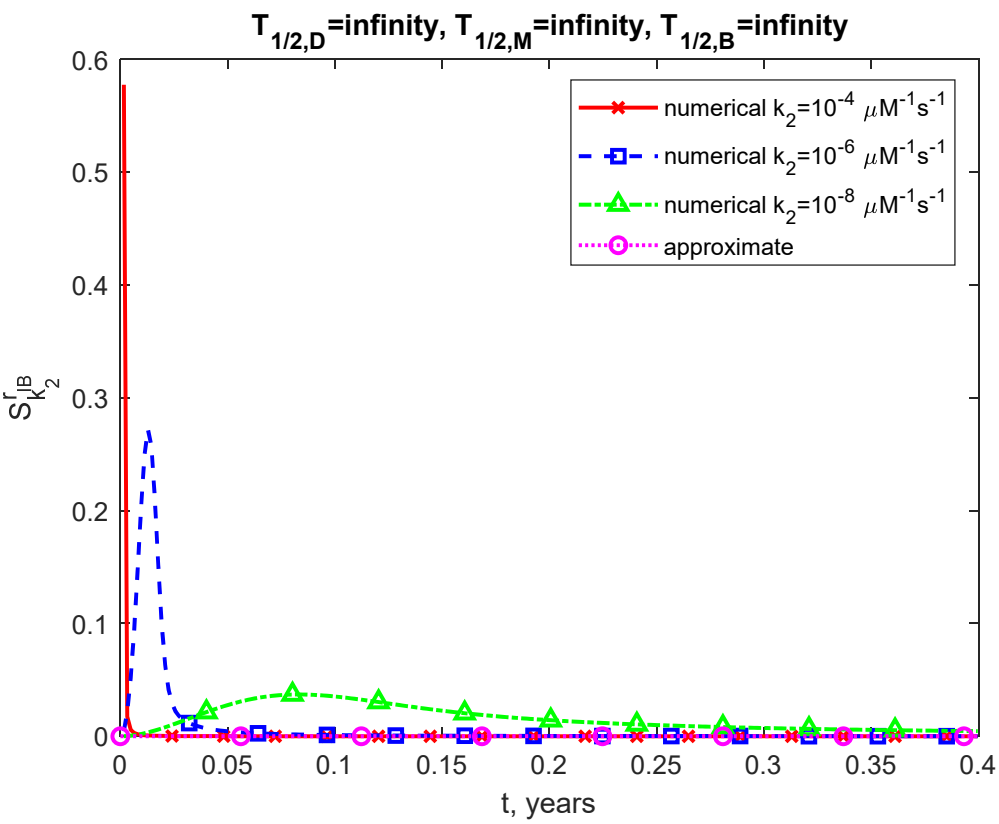

Figure 8a,b

(c)

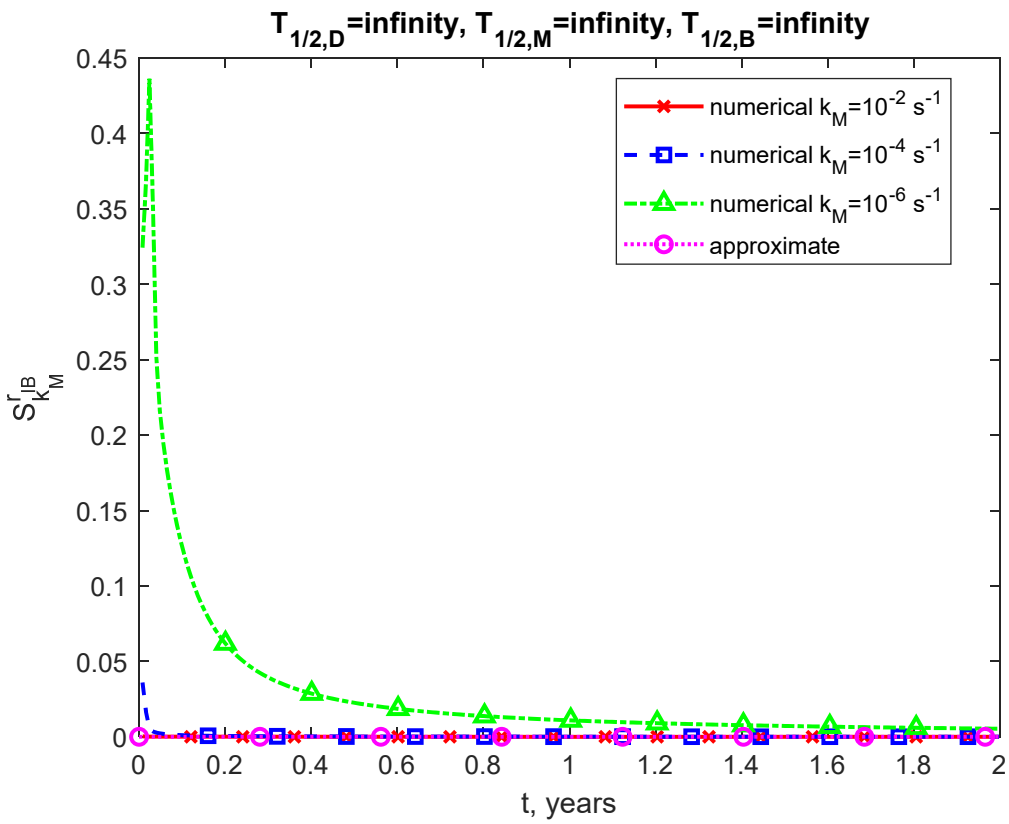
T1/2,D=infinity, T1/2,M=infinity, T1/2,B=infinity
numerical kM=10-2 s-1
numerical kM=10-4 s-1
numerical kM=10-6 s-1
approximate
S r kM IB
t, years
0.45
0.4
0.35
0.3
0.25
0.2
0.15
0.1
0.05
0
0
0.2
0.4
0.6
0.8
1
1.2
1.4
1.6
1.8
2

Figure 8c

Simulating growth of TDP-43 cytosolic inclusion bodies in neuron soma

Andrey V. Kuznetsov

Department of Mechanical and Aerospace Engineering, North Carolina State University,

Raleigh, NC 27695-7910, USA; e-mail: avkuznet@ncsu.edu

Supplemental Materials

S1. Supplemental tables

Table S1. Data extracted from Table 2 of [21], presenting best-fit values of rate constants, k_1 and k_2, used for simulating the aggregation of diverse proteins by the F-W model, $A \xrightarrow{k_1} B$, $A + B \xrightarrow{k_2} 2B$ (A denotes monomers and B denotes aggregates). The data reported in [21] has been converted into SI units to establish representative ranges for k_1 and k_2. This was done because values for k_1 and k_2 specific to TDP-43 are not available in the literature.

Entry (same as in [21])	System	k_1, s^{-1}	k_2, μM^{-1} s^{-1}	Reference
1	amyloid β	2.2×10^{-9}	6.4×10^{-7}	[34]
2	amyloid β	1×10^{-4}	1.2×10^{-5}	[35]
3	amyloid β	1.7×10^{-10}	8.3×10^{-2}	[36]
4	amyloid β, 1 mM peptide	2.8×10^{-8}	1.6×10^{-2}	[37]
5	amyloid β, [Zn]:[peptide]= 0.2	2.3×10^{-7}	1.8×10^{-2}	[37]
6	amyloid β, [Zn]:[peptide]= 0.4	4.4×10^{-8}	1.9×10^{-2}	[37]
7	amyloid β, Aβ 1-16	8.1×10^{-8}	2.1×10^{-5}	[38]
8	amyloid β, Aβ 5-16	2.4×10^{-8}	4.1×10^{-5}	[38]
9	α-synuclein	1.1×10^{-8}	1.1×10^{-6}	[39]
10	α-synuclein	2.8×10^{-7}	3.1×10^{-4}	[40]
11	polyglutamine	7.2×10^{-7}	6.4×10^{-8}	[41]
12	polyglutamine	2.8×10^{-7}	3.6×10^{-6}	[42]
13	β-microglobulin	1.7×10^{-13}	1.5×10^{-4}	[43]
14	D67H lysozyme	3.1×10^{-5}	3.9×10^{-5}	[44]

S2. Supplemental figures

Figs. S1-S9 and Figs. S10-S18 present illustrations of the concentrations of TDP-43 dimers [*D*], monomers [*M*], and aggregates [*B*] under different scenarios. Figs. S1-S9 depict a situation with infinite half-lives of TDP-43 dimers, monomers, and aggregates, while Figs. S10-S18 represent a scenario with physiologically relevant half-lives of these proteins. The numerical solution is obtained by solving Eqs. (4)-(6) numerically, with the initial condition (7). The approximate analytical solution depicted in Figs. S1-S9 is computed utilizing Eqs. (8), (12), and (11).

(a)

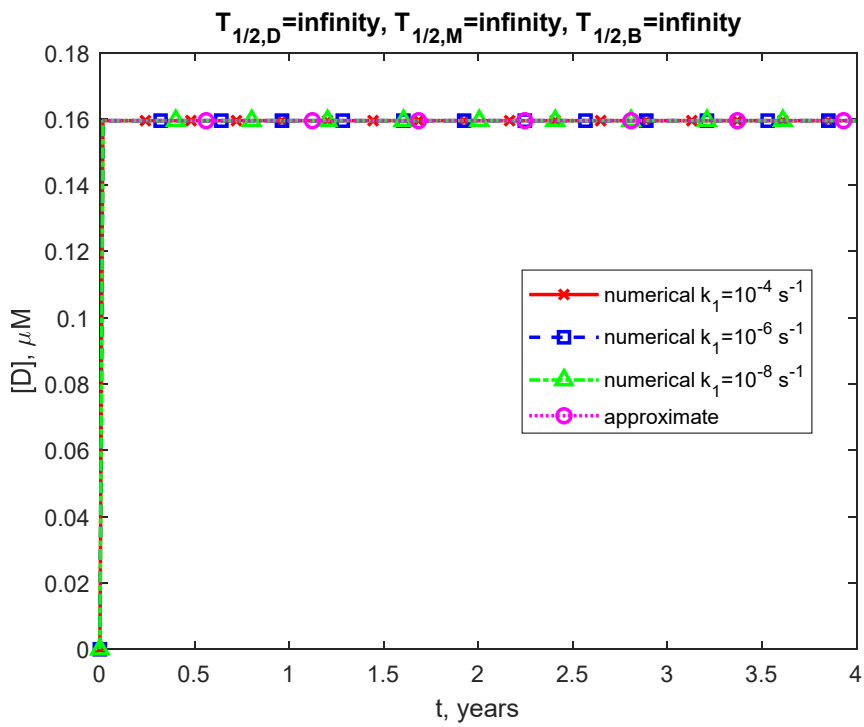

(b)

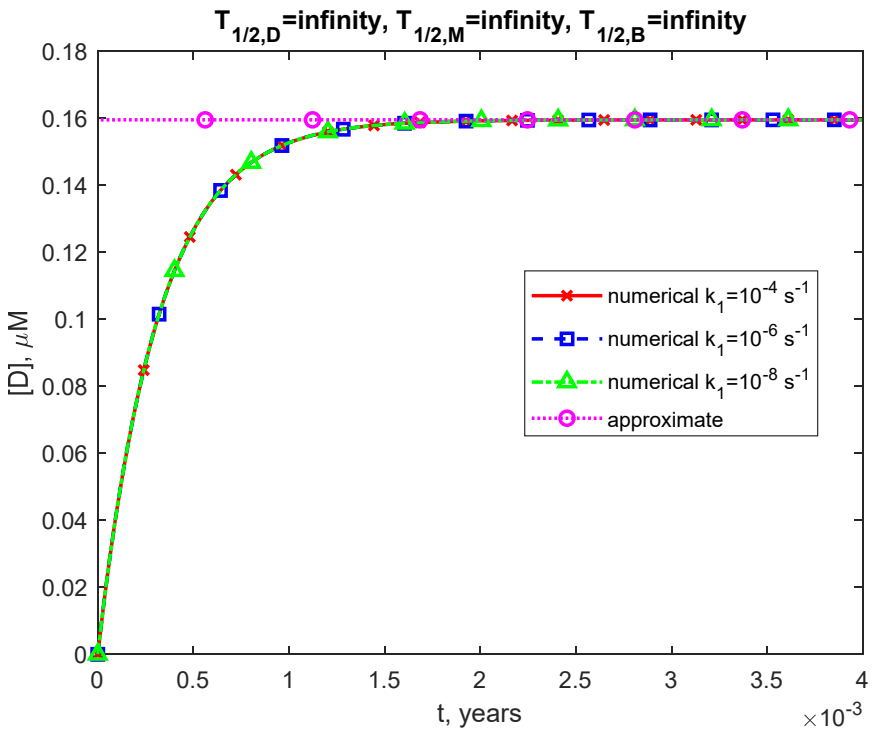

Fig. S1. (a) Molar concentration of TDP-43 dimers, [*D*], over time (in years). (b) Similar to Fig. S1a but focusing on a specific time range of [0 0.004 year] on the *x*-axis. The numerical solution is obtained by solving Eqs. (4)-(6) numerically with the initial condition (7). The approximate solution is determined by employing Eq. (8). The presented scenario assumes dysfunctional protein degradation machinery with $T_{1/2,D} \to \infty$, $T_{1/2,M} \to \infty$, and $T_{1/2,B} \to \infty$. The results are displayed for three values of k_1. $k_2 = 10^{-6}$ μM^{-1} s^{-1} and $k_M = 10^{-4}$ s^{-1}.

(a)

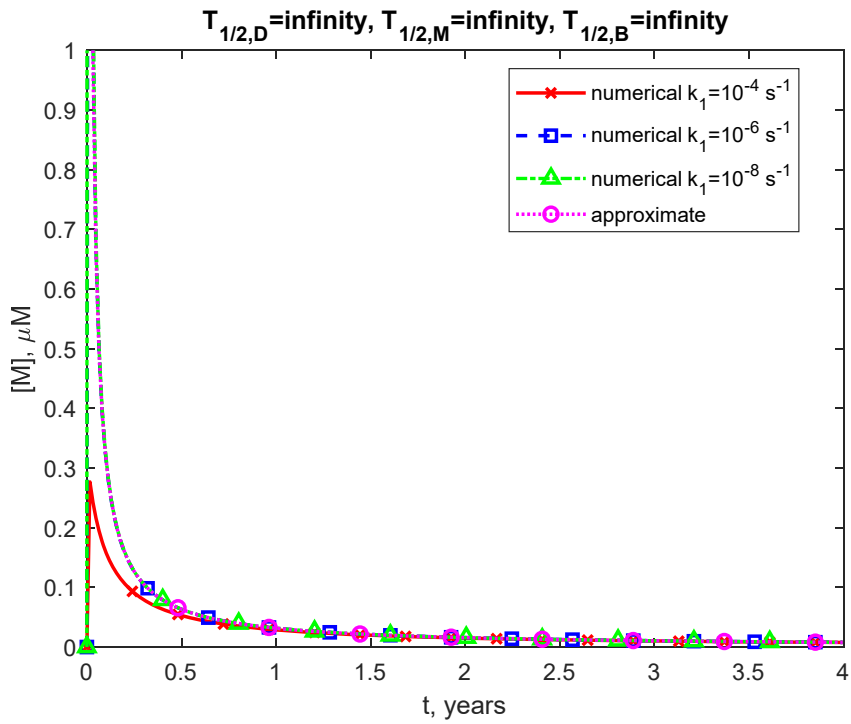

(b)

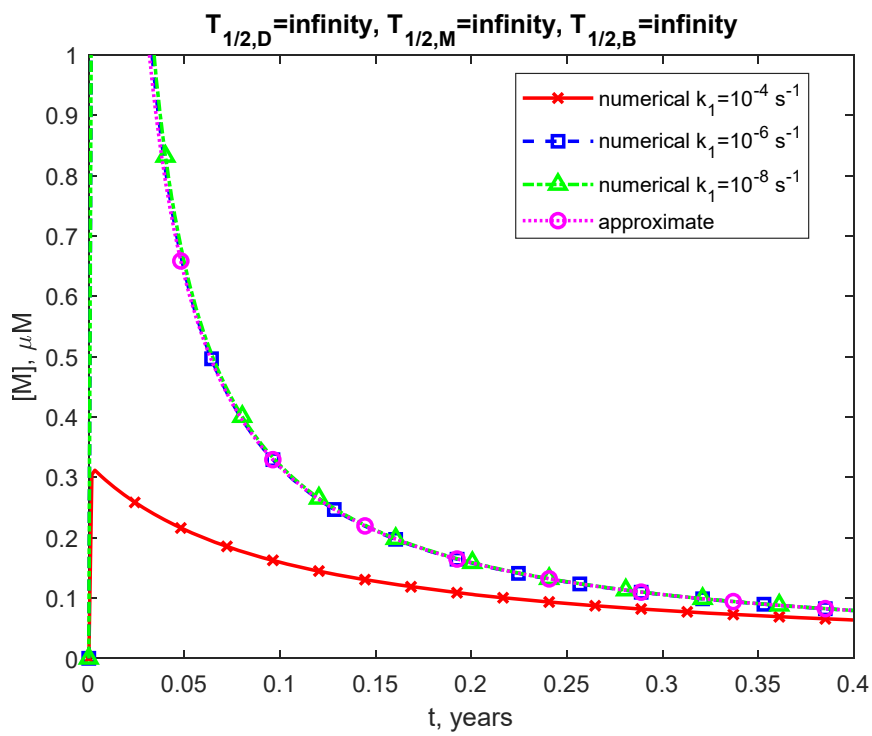

Fig. S2. (a) Molar concentration of TDP-43 monomers, [*M*], over time (in years). (b) Similar to Fig. S2a but focusing on a specific time range of [0 0.4 year] on the *x*-axis. The numerical solution is obtained by

solving Eqs. (4)-(6) numerically with the initial condition (7). The approximate solution is determined by employing Eq. (12). The presented scenario assumes dysfunctional protein degradation machinery with $T_{1/2,D} \to \infty$, $T_{1/2,M} \to \infty$, and $T_{1/2,B} \to \infty$. The results are displayed for three values of k_1. $k_2 = 10^{-6}$ μM^{-1} s^{-1} and $k_M = 10^{-4}$ s^{-1}.

(a)

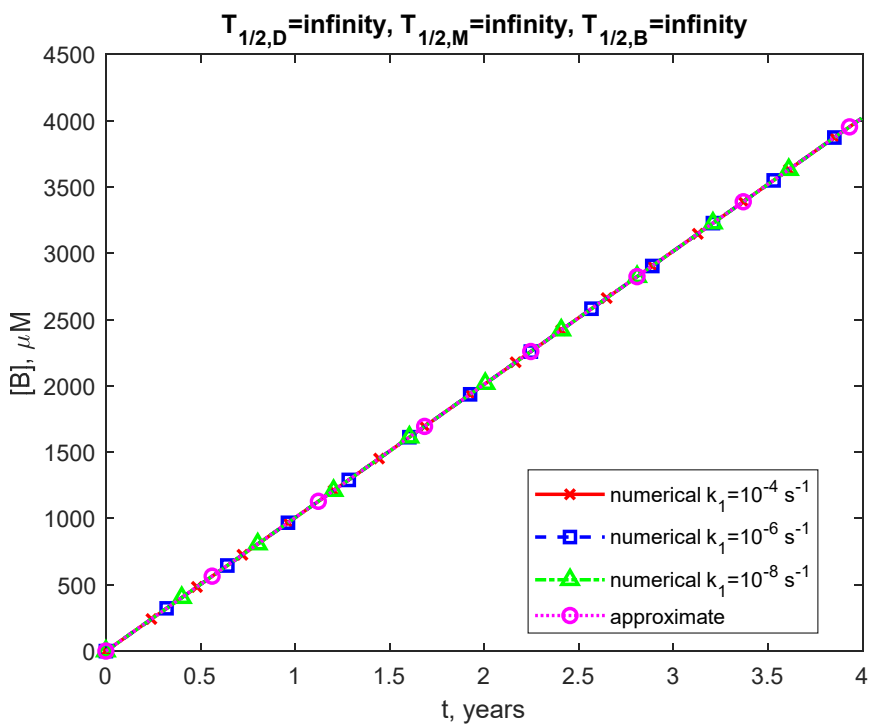

(b)

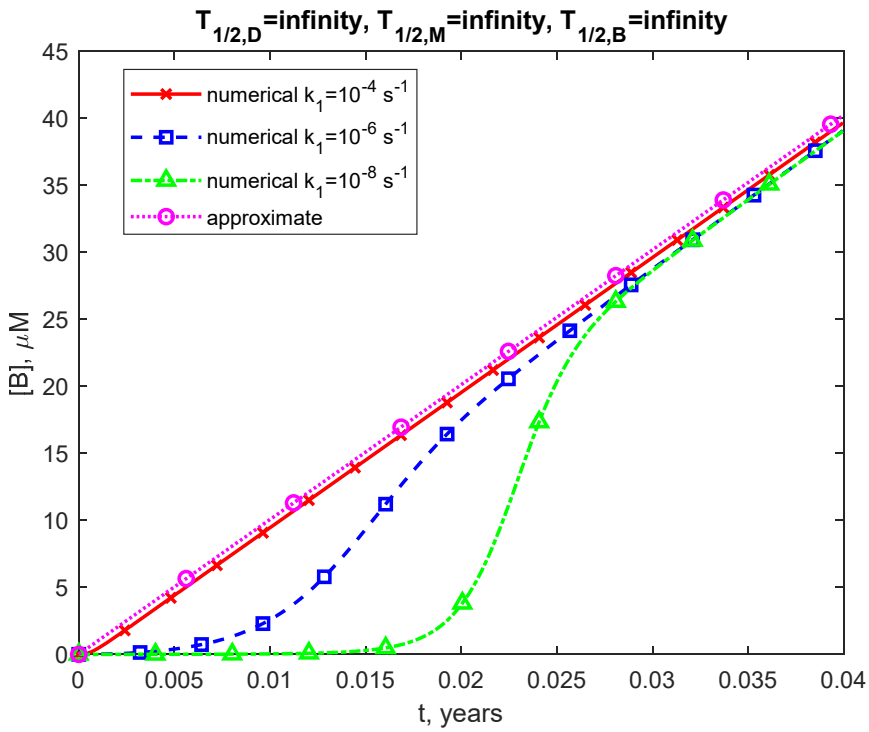

Fig. S3. (a) Molar concentration of TDP-43 aggregates, [*B*], over time (in years). (b) Similar to Fig. S3a but focusing on a specific time range of [0 0.04 year] on the *x*-axis. The numerical solution is obtained by solving Eqs. (4)-(6) numerically with the initial condition (7). The approximate solution is determined by employing Eq. (11). The presented scenario assumes dysfunctional protein degradation machinery with $T_{1/2,D} \to \infty$, $T_{1/2,M} \to \infty$, and $T_{1/2,B} \to \infty$. The results are displayed for three values of k_1. $k_2 = 10^{-6}$ μM^{-1} s^{-1} and $k_M = 10^{-4}$ s^{-1}.

(a)

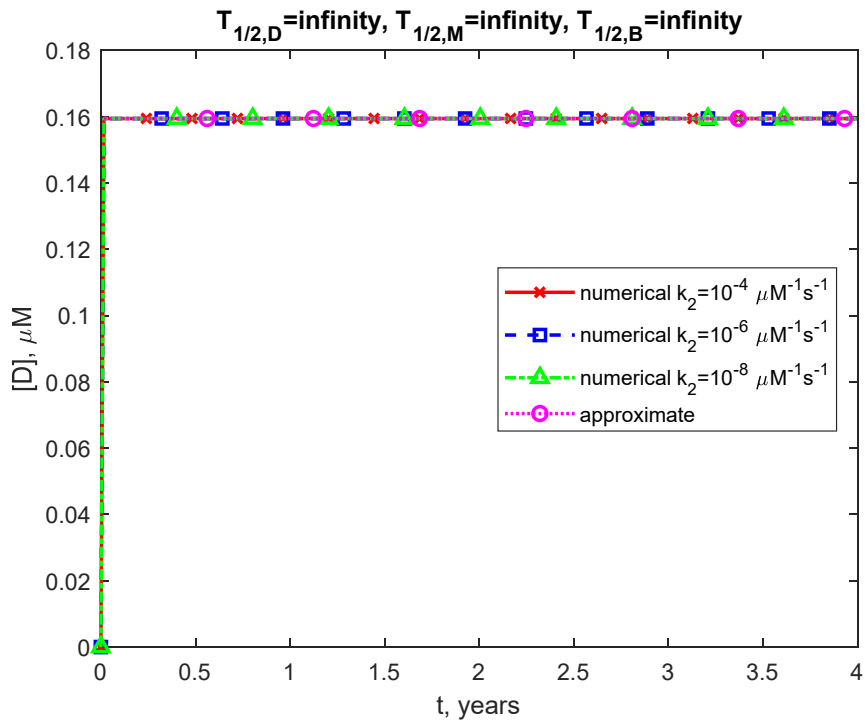

(b)

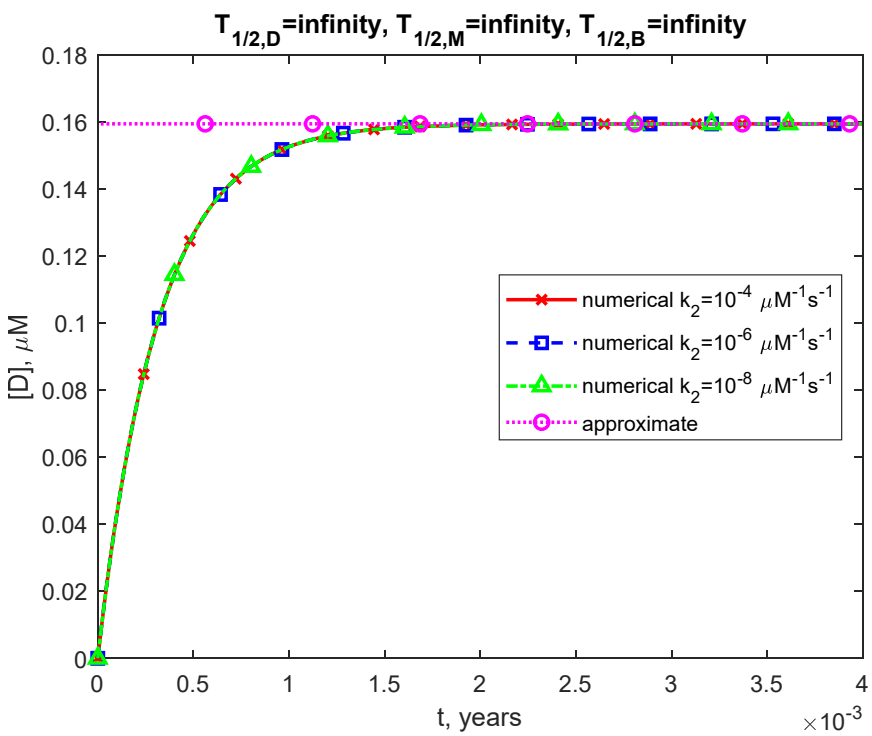

Fig. S4. (a) Molar concentration of TDP-43 dimers, [*D*], over time (in years). (b) Similar to Fig. S4a but focusing on a specific time range of [0 0.004 year] on the *x*-axis. The numerical solution is obtained by

solving Eqs. (4)-(6) numerically with the initial condition (7). The approximate solution is determined by employing Eq. (8). The presented scenario assumes dysfunctional protein degradation machinery with $T_{1/2,D} \to \infty$, $T_{1/2,M} \to \infty$, and $T_{1/2,B} \to \infty$. The results are displayed for three values of k_2. $k_1 = 10^{-6}$ s^{-1} and $k_M = 10^{-4}$ s^{-1}.

(a)

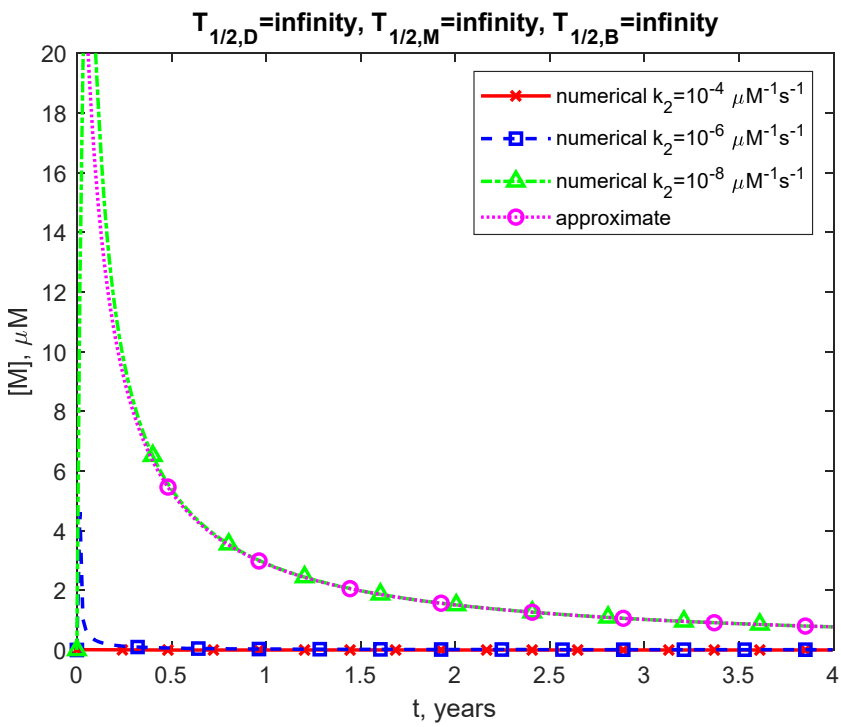

(b)

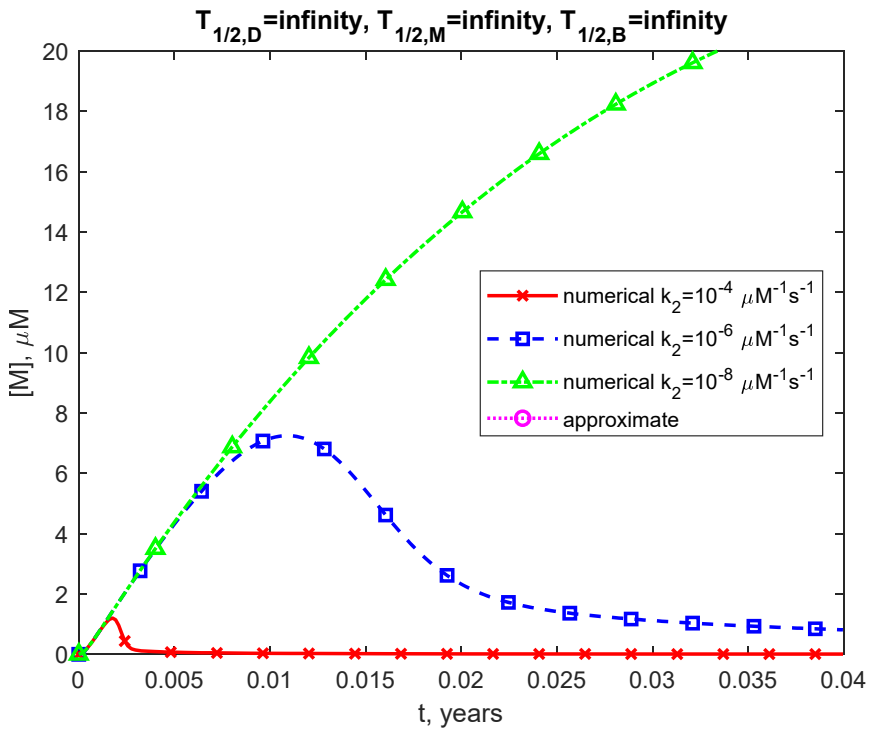

Fig. S5. (a) Molar concentration of TDP-43 monomers, [*M*], over time (in years). (b) Similar to Fig. S5a but focusing on a specific time range of [0 0.04 year] on the *x*-axis. The numerical solution is obtained by solving Eqs. (4)-(6) numerically with the initial condition (7). The approximate solution is determined by employing Eq. (12). The presented scenario assumes dysfunctional protein degradation machinery with $T_{1/2,D} \to \infty$, $T_{1/2,M} \to \infty$, and $T_{1/2,B} \to \infty$. The results are displayed for three values of k_2. $k_1 = 10^{-6}$ s^{-1} and $k_M = 10^{-4}$ s^{-1}.

(a)

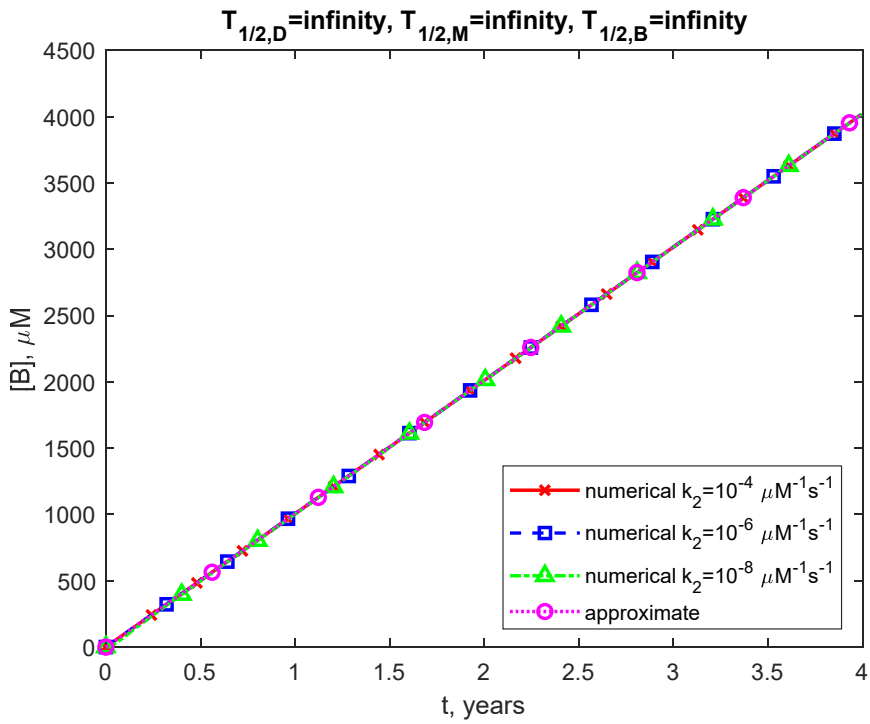

(b)

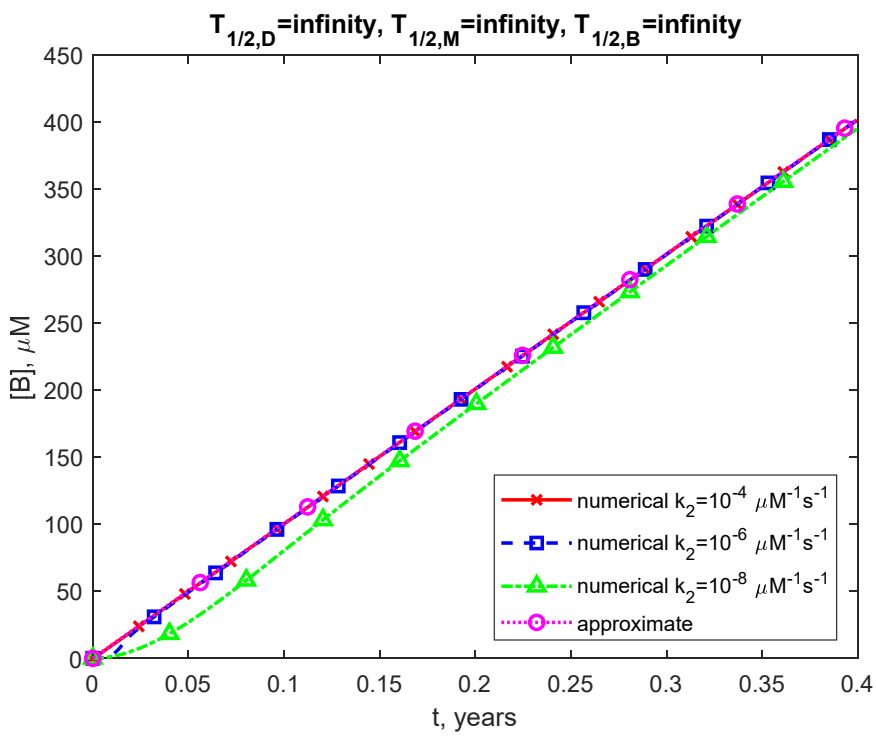

Fig. S6. (a) Molar concentration of TDP-43 aggregates, [*B*], over time (in years). (b) Similar to Fig. S6a but focusing on a specific time range of [0 0.4 year] on the *x*-axis. The numerical solution is obtained by

solving Eqs. (4)-(6) numerically with the initial condition (7). The approximate solution is determined by employing Eq. (11). The presented scenario assumes dysfunctional protein degradation machinery with $T_{1/2,D} \to \infty$, $T_{1/2,M} \to \infty$, and $T_{1/2,B} \to \infty$. The results are displayed for three values of k_2. $k_1 = 10^{-6}$ s^{-1} and $k_M = 10^{-4}$ s^{-1}.

(a)

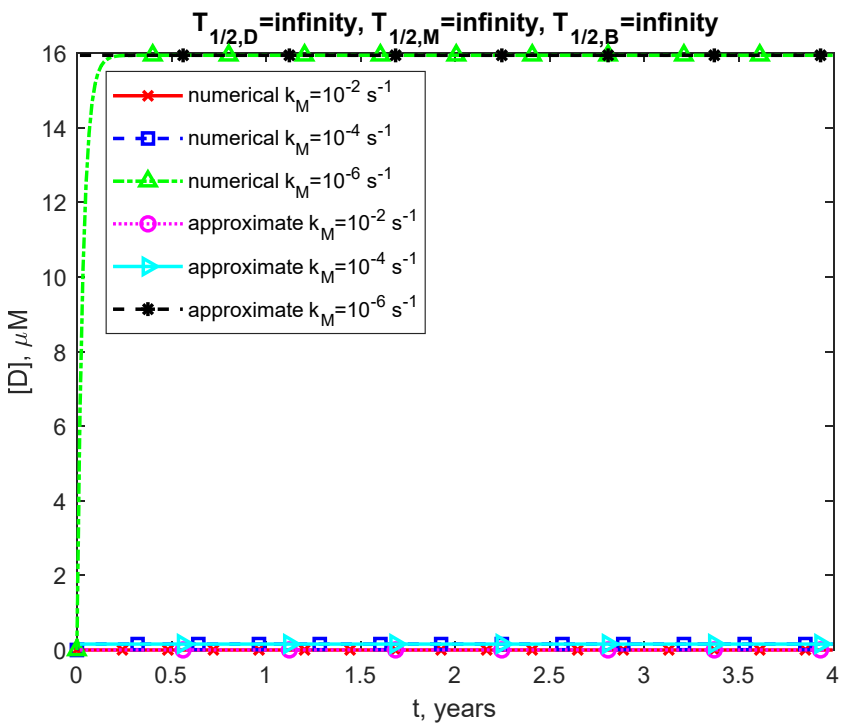

(b)

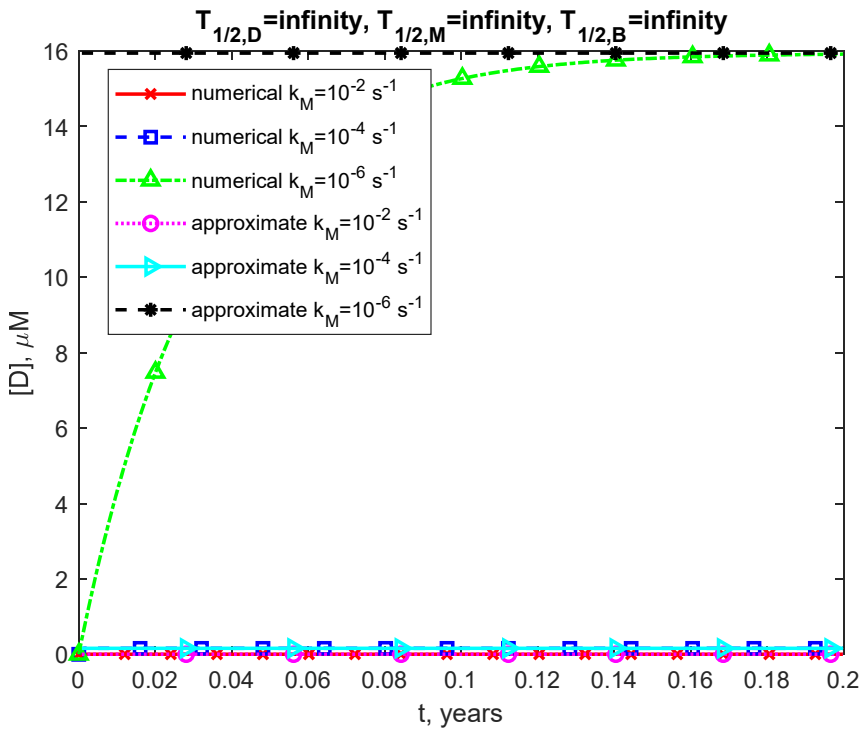

Fig. S7. (a) Molar concentration of TDP-43 dimers, [*D*], over time (in years). (b) Similar to Fig. S7a but focusing on a specific time range of [0 0.2 year] on the *x*-axis. The numerical solution is obtained by solving Eqs. (4)-(6) numerically with the initial condition (7). The approximate solution is determined by employing Eq. (8). The presented scenario assumes dysfunctional protein degradation machinery with $T_{1/2,D} \to \infty$, $T_{1/2,M} \to \infty$, and $T_{1/2,B} \to \infty$. The results are displayed for three values of k_M. $k_1 = 10^{-6}$ s^{-1} and $k_2 = 10^{-6}$ μM^{-1} s^{-1}.

(a)

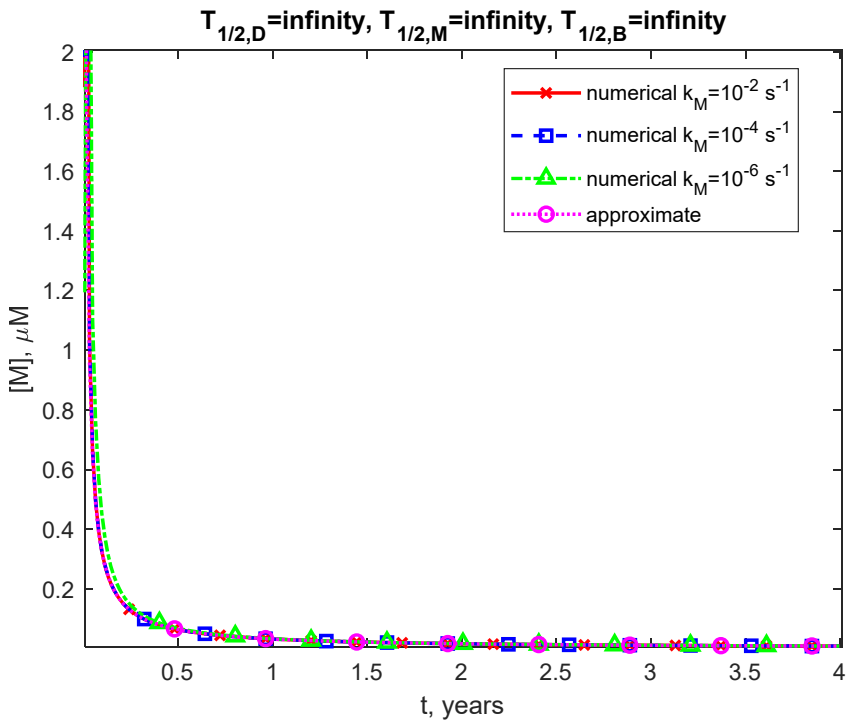

(b)

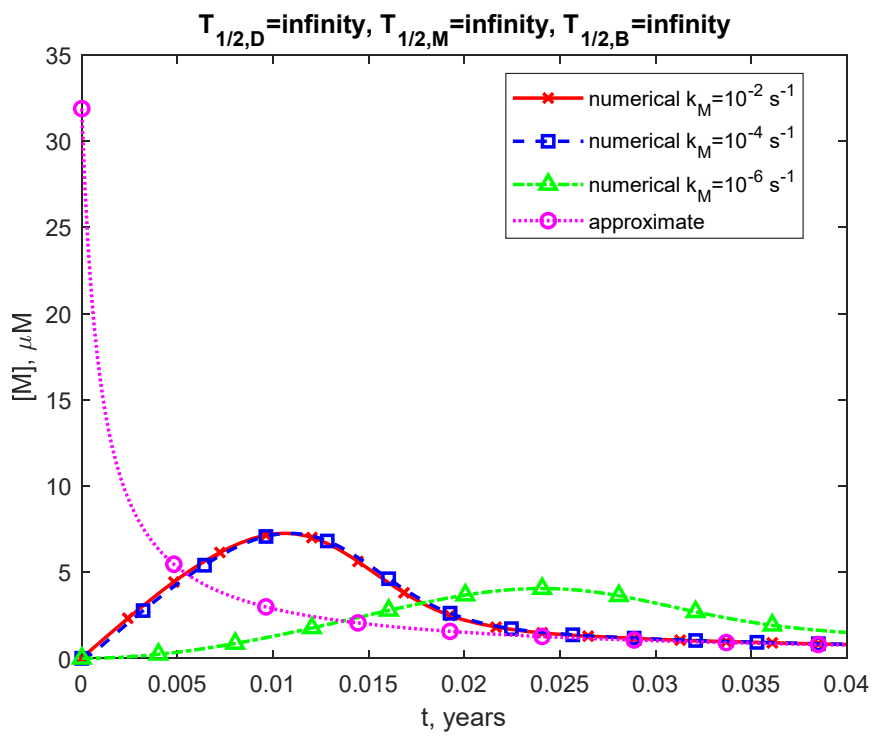

Fig. S8. (a) Molar concentration of TDP-43 monomers, [*M*], over time (in years). (b) Similar to Fig. S8a but focusing on a specific time range of [0 0.04 year] on the *x*-axis. The numerical solution is obtained by

solving Eqs. (4)-(6) numerically with the initial condition (7). The approximate solution is determined by employing Eq. (12). The presented scenario assumes dysfunctional protein degradation machinery with $T_{1/2,D} \to \infty$, $T_{1/2,M} \to \infty$, and $T_{1/2,B} \to \infty$. The results are displayed for three values of k_M. $k_1 = 10^{-6}$ s^{-1} and $k_2 = 10^{-6}$ μM^{-1} s^{-1}.

(a)

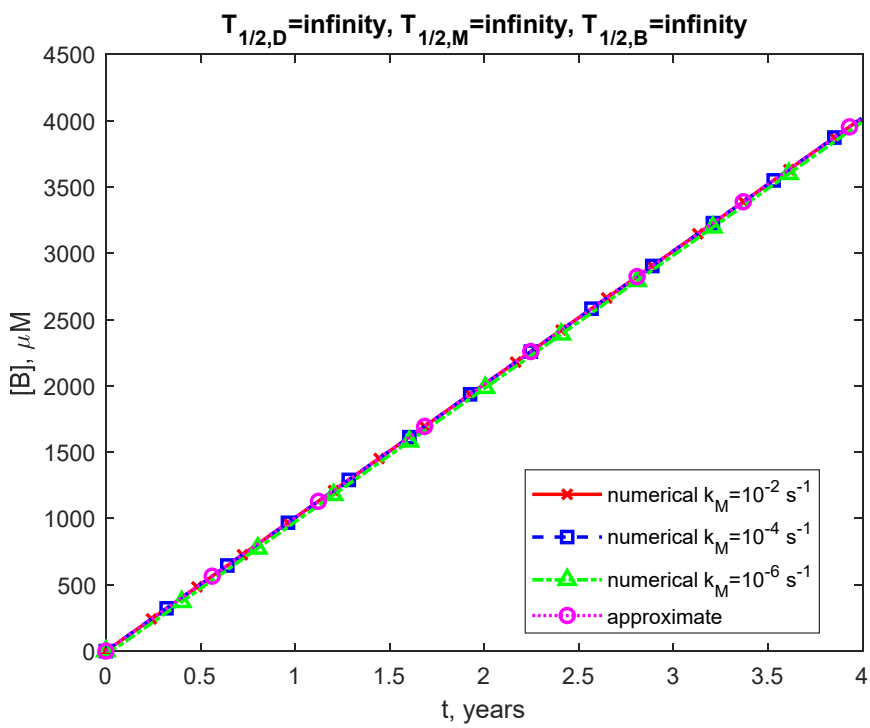

(b)

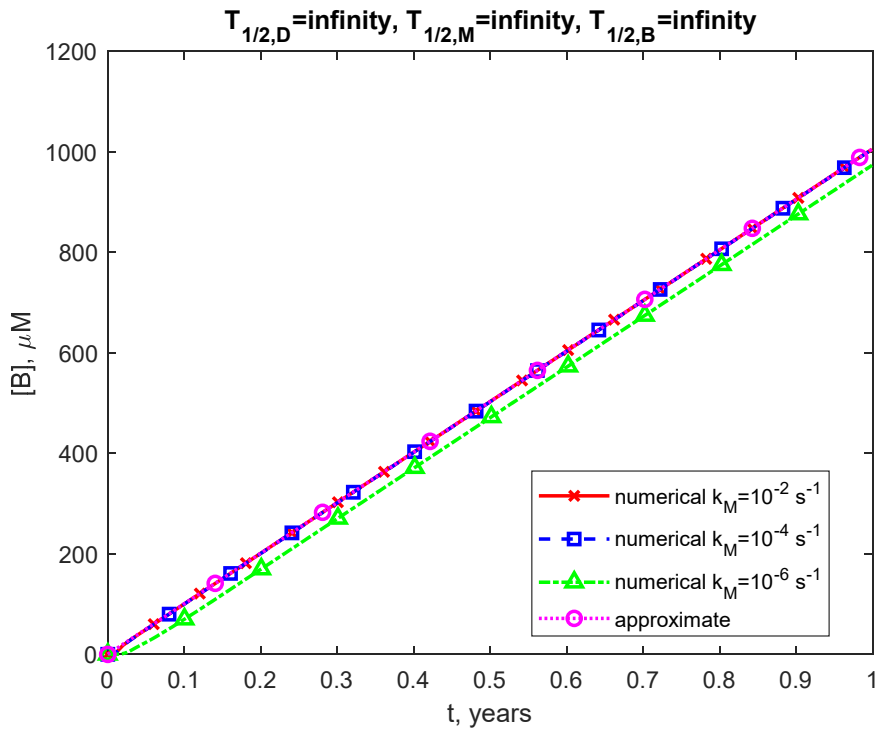

Fig. S9. (a) Molar concentration of TDP-43 aggregates, [*B*], over time (in years). (b) Similar to Fig. S9a but focusing on a specific time range of [0 1 year] on the *x*-axis. The numerical solution is obtained by solving Eqs. (4)-(6) numerically with the initial condition (7). The approximate solution is determined by employing Eq. (11). The presented scenario assumes dysfunctional protein degradation machinery with $T_{1/2,D} \to \infty$, $T_{1/2,M} \to \infty$, and $T_{1/2,B} \to \infty$. The results are displayed for three values of k_M. $k_1 = 10^{-6}$ s^{-1} and $k_2 = 10^{-6}$ μM^{-1} s^{-1}.

(a)

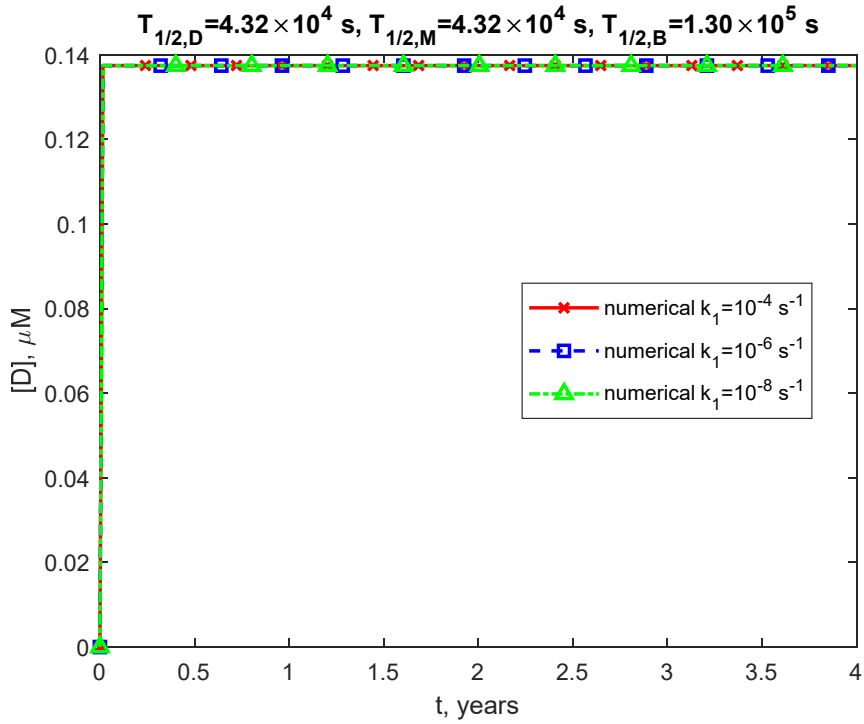

(b)

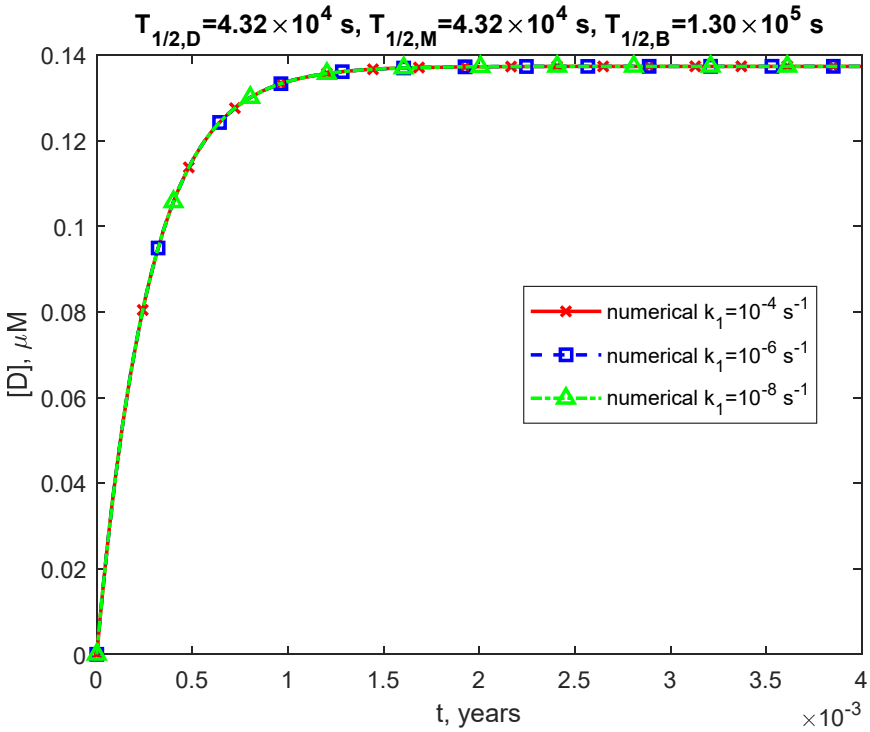

Fig. S10. (a) Molar concentration of TDP-43 dimers, [*D*], over time (in years). (b) Similar to Fig. S10a but focusing on a specific time range of [0 0.004 year] on the *x*-axis. The numerical solution is obtained

by solving Eqs. (4)-(6) numerically with the initial condition (7). The presented scenario assumes physiologically relevant values for the half-lives of TDP-43 dimers, monomers, and aggregates. $T_{1/2,D} = 4.32\times10^4$ s, $T_{1/2,M} = 4.32\times10^4$ s, and $T_{1/2,B} = 1.30\times10^5$ s. The approximate solution is not displayed as it applies exclusively to the scenario involving infinite half-lives of TDP-43 dimers, monomers, and aggregates. The results are displayed for three values of k_1. $k_2 = 10^{-6}$ μM^{-1} s^{-1} and $k_M = 10^{-4}$ s^{-1}.

(a)

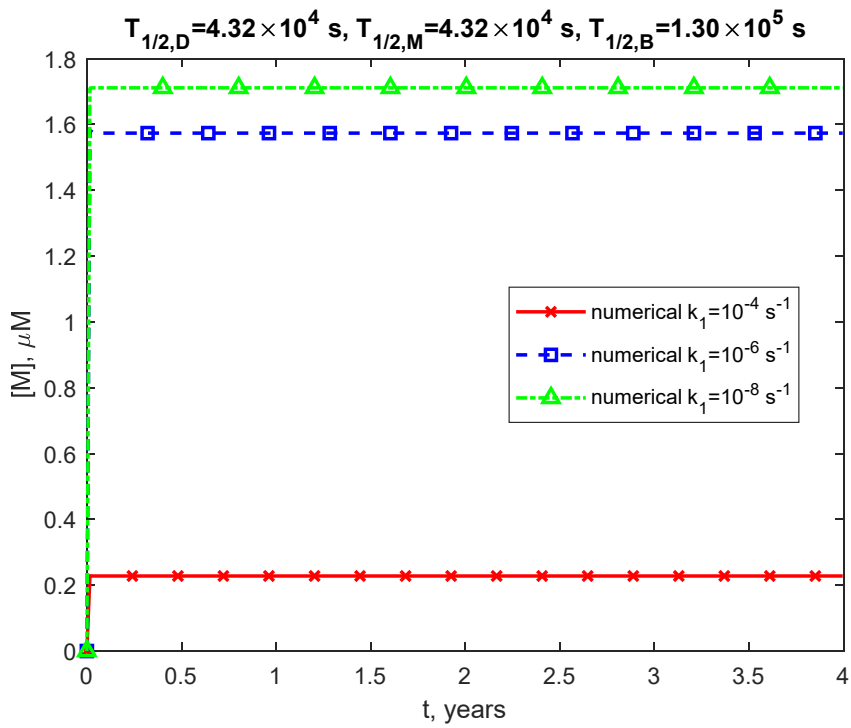

(b)

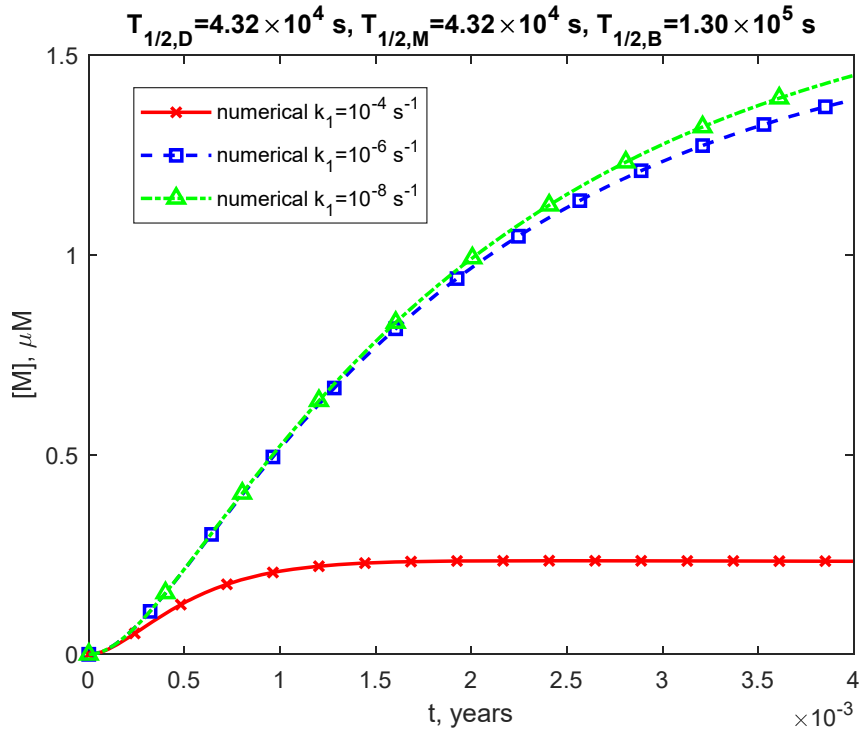

Fig. S11. (a) Molar concentration of TDP-43 monomers, [*M*], over time (in years). (b) Similar to Fig. S11a but focusing on a specific time range of [0 0.004 year] on the *x*-axis. The numerical solution is obtained by solving Eqs. (4)-(6) numerically with the initial condition (7). The presented scenario assumes physiologically relevant values for the half-lives of TDP-43 dimers, monomers, and aggregates. $T_{1/2,D} = 4.32\times10^4$ s, $T_{1/2,M} = 4.32\times10^4$ s, and $T_{1/2,B} = 1.30\times10^5$ s. The approximate solution is not displayed as it applies exclusively to the scenario involving infinite half-lives of TDP-43 dimers, monomers, and aggregates. The results are displayed for three values of k_1. $k_2 = 10^{-6}$ μM^{-1} s^{-1} and $k_M = 10^{-4}$ s^{-1}.

(a)

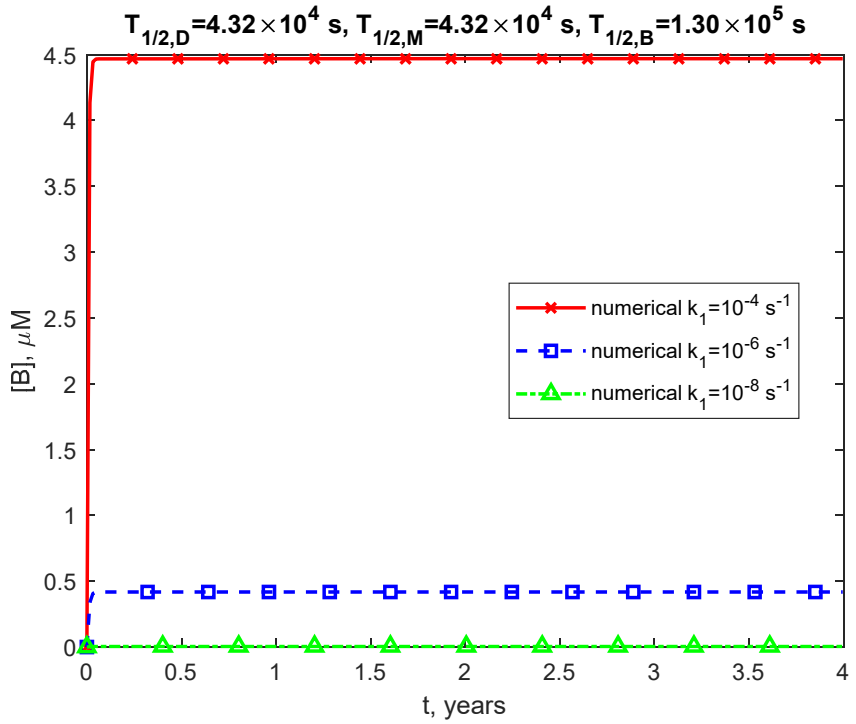

(b)

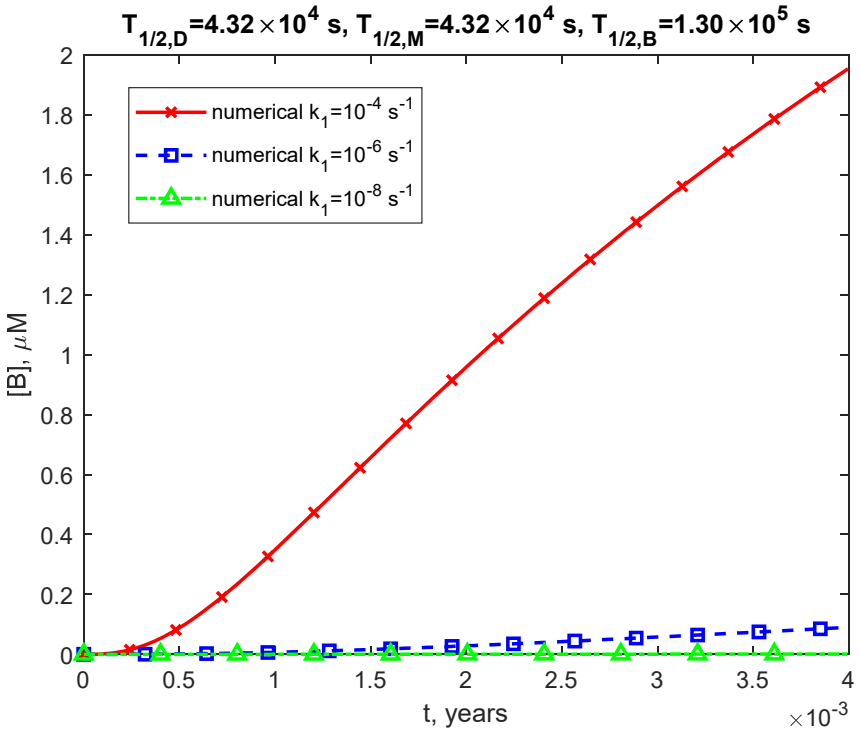

Fig. S12. (a) Molar concentration of TDP-43 aggregates, [*B*], over time (in years). (b) Similar to Fig. S12a but focusing on a specific time range of [0 0.004 year] on the *x*-axis. The numerical solution is

obtained by solving Eqs. (4)-(6) numerically with the initial condition (7). The presented scenario assumes physiologically relevant values for the half-lives of TDP-43 dimers, monomers, and aggregates. $T_{1/2,D} = 4.32\times10^4$ s, $T_{1/2,M} = 4.32\times10^4$ s, and $T_{1/2,B} = 1.30\times10^5$ s. The approximate solution is not displayed as it applies exclusively to the scenario involving infinite half-lives of TDP-43 dimers, monomers, and aggregates. The results are displayed for three values of k_1. $k_2 = 10^{-6}$ μM^{-1} s^{-1} and $k_M = 10^{-4}$ s^{-1}.

(a)

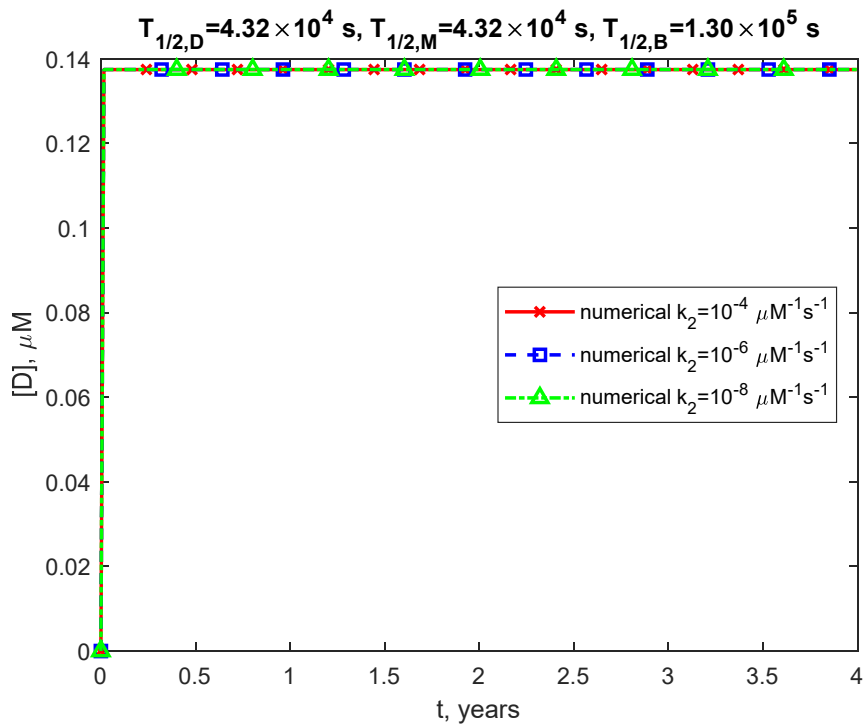

(b)

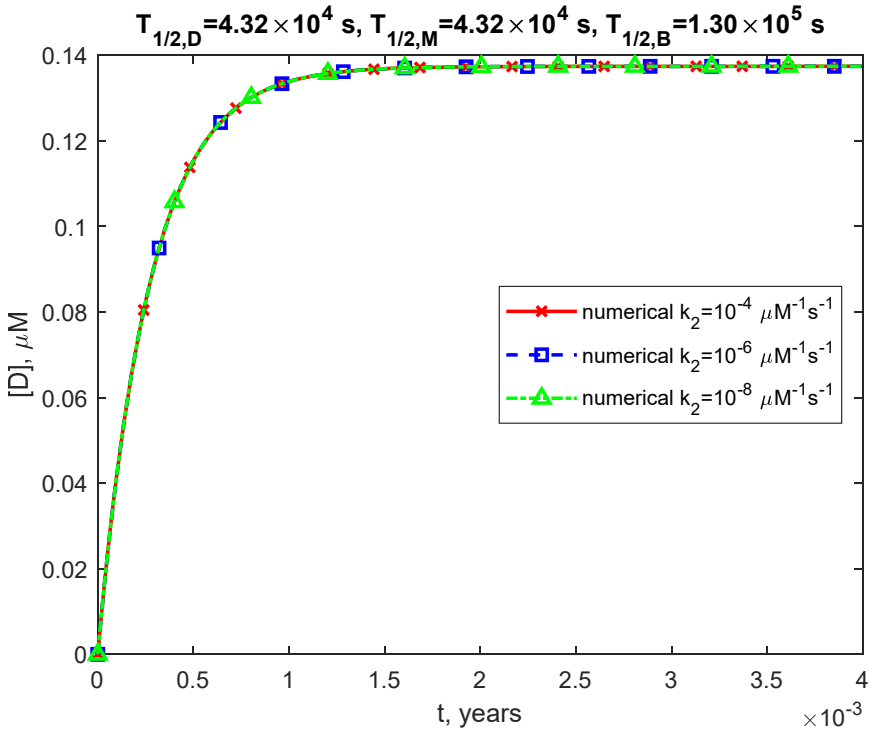

Fig. S13. (a) Molar concentration of TDP-43 dimers, [*D*], over time (in years). (b) Similar to Fig. S13a but focusing on a specific time range of [0 0.004 year] on the *x*-axis. The numerical solution is obtained by solving Eqs. (4)-(6) numerically with the initial condition (7). The presented scenario assumes physiologically relevant values for the half-lives of TDP-43 dimers, monomers, and aggregates. $T_{1/2,D} = 4.32\times10^4$ s, $T_{1/2,M} = 4.32\times10^4$ s, and $T_{1/2,B} = 1.30\times10^5$ s. The approximate solution is not displayed as it applies exclusively to the scenario involving infinite half-lives of TDP-43 dimers, monomers, and aggregates. The results are displayed for three values of k_2. $k_1 = 10^{-6}$ s^{-1} and $k_M = 10^{-4}$ s^{-1}.

(a)

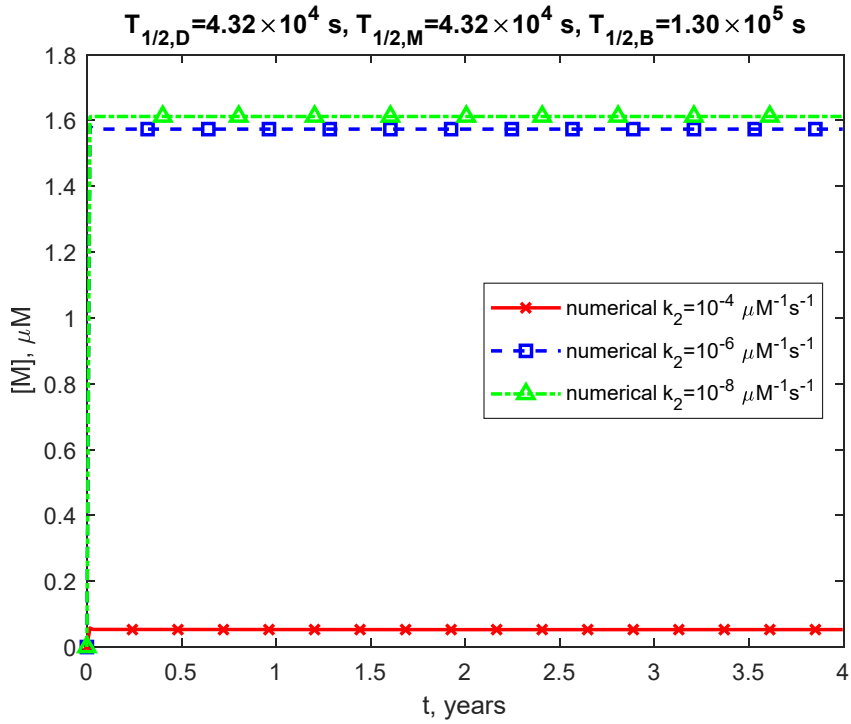

(b)

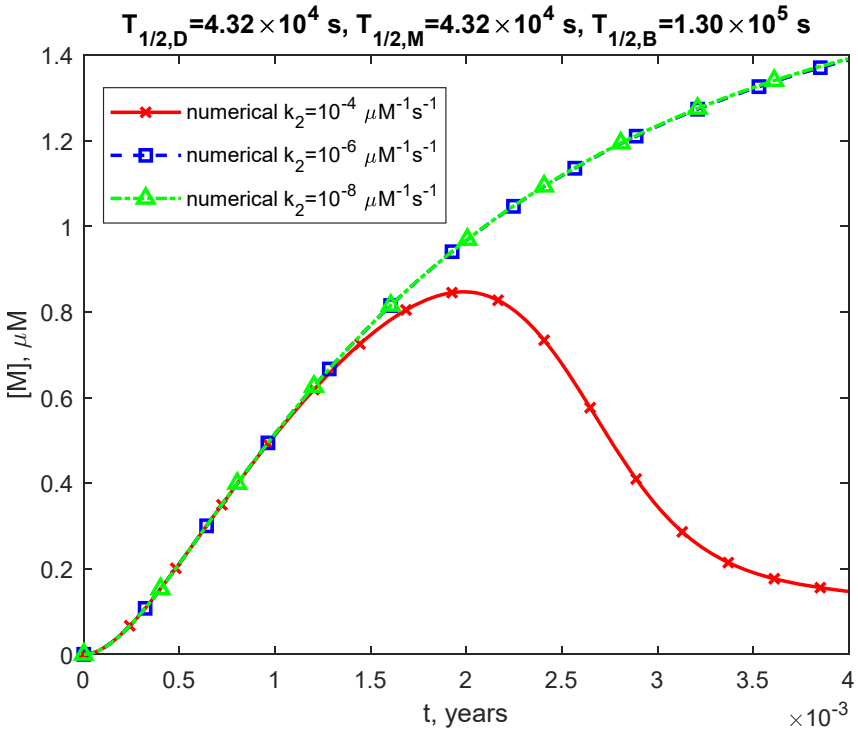

Fig. S14. (a) Molar concentration of TDP-43 monomers, [*M*], over time (in years). (b) Similar to Fig. S14a but focusing on a specific time range of [0 0.004 year] on the *x*-axis. The numerical solution is

obtained by solving Eqs. (4)-(6) numerically with the initial condition (7). The presented scenario assumes physiologically relevant values for the half-lives of TDP-43 dimers, monomers, and aggregates. $T_{1/2,D} = 4.32\times10^4$ s, $T_{1/2,M} = 4.32\times10^4$ s, and $T_{1/2,B} = 1.30\times10^5$ s. The approximate solution is not displayed as it applies exclusively to the scenario involving infinite half-lives of TDP-43 dimers, monomers, and aggregates. The results are displayed for three values of k_2. $k_1 = 10^{-6}$ s^{-1} and $k_M = 10^{-4}$ s^{-1}.

(a)

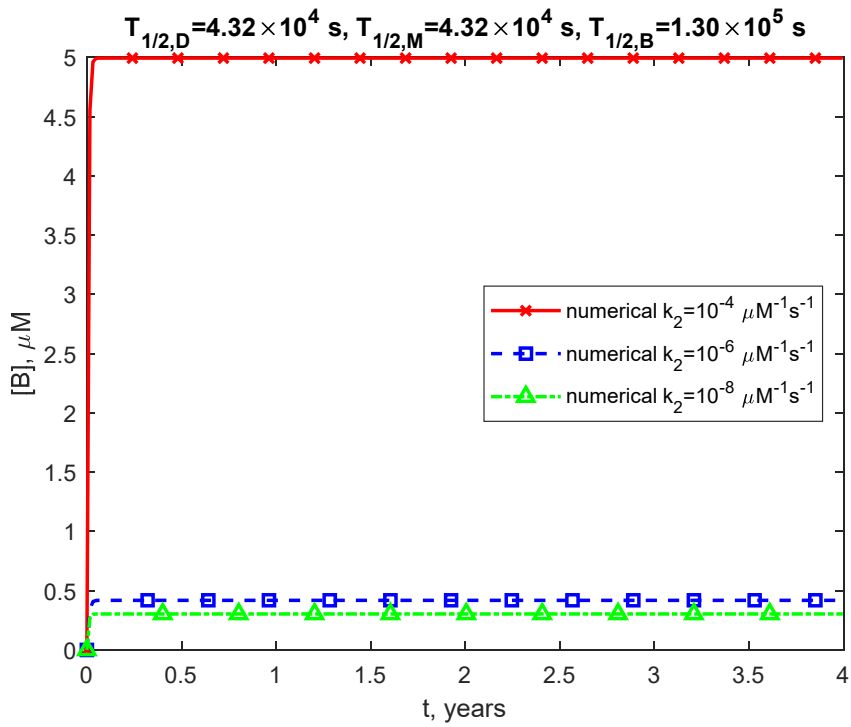

(b)

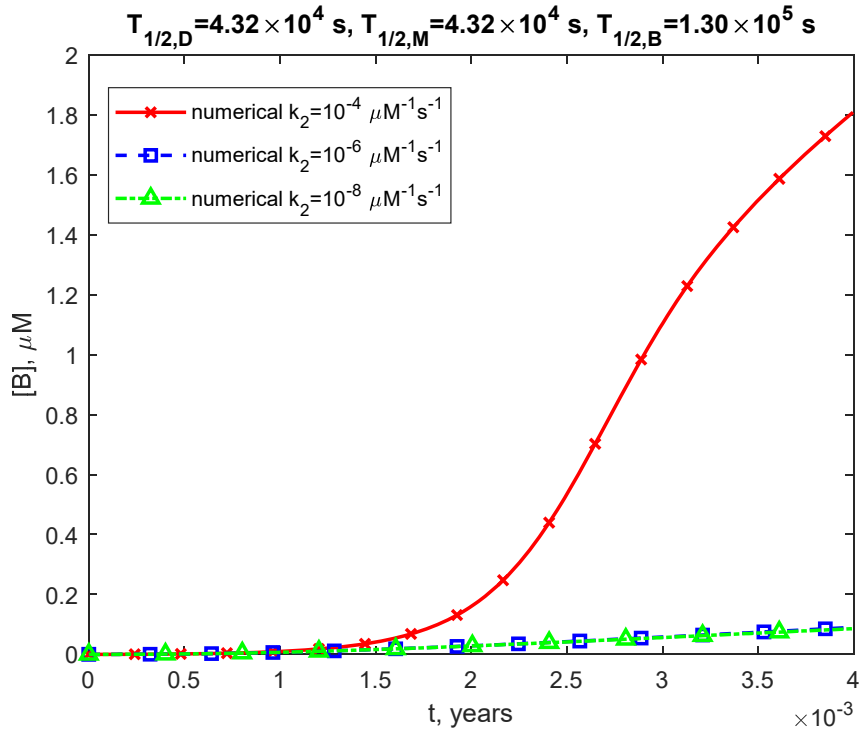

Fig. S15. (a) Molar concentration of TDP-43 aggregates, [*B*], over time (in years). (b) Similar to Fig. S15a but focusing on a specific time range of [0 0.004 year] on the *x*-axis. The numerical solution is obtained by solving Eqs. (4)-(6) numerically with the initial condition (7). The presented scenario assumes physiologically relevant values for the half-lives of TDP-43 dimers, monomers, and aggregates. $T_{1/2,D} = 4.32\times10^4$ s, $T_{1/2,M} = 4.32\times10^4$ s, and $T_{1/2,B} = 1.30\times10^5$ s. The approximate solution is not displayed as it applies exclusively to the scenario involving infinite half-lives of TDP-43 dimers, monomers, and aggregates. The results are displayed for three values of k_2. $k_1 = 10^{-6}$ s^{-1} and $k_M = 10^{-4}$ s^{-1}.

(a)

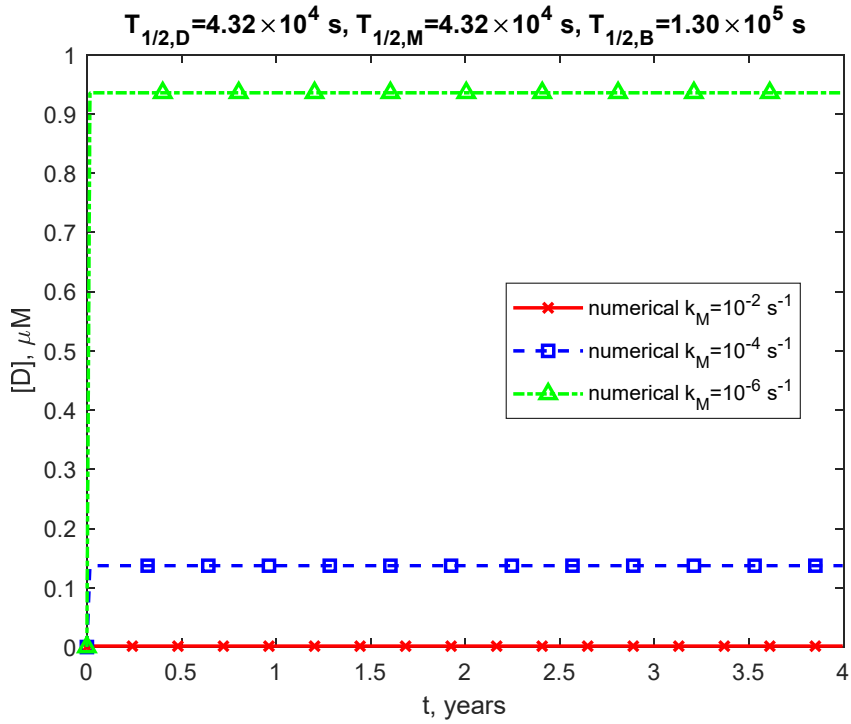

(b)

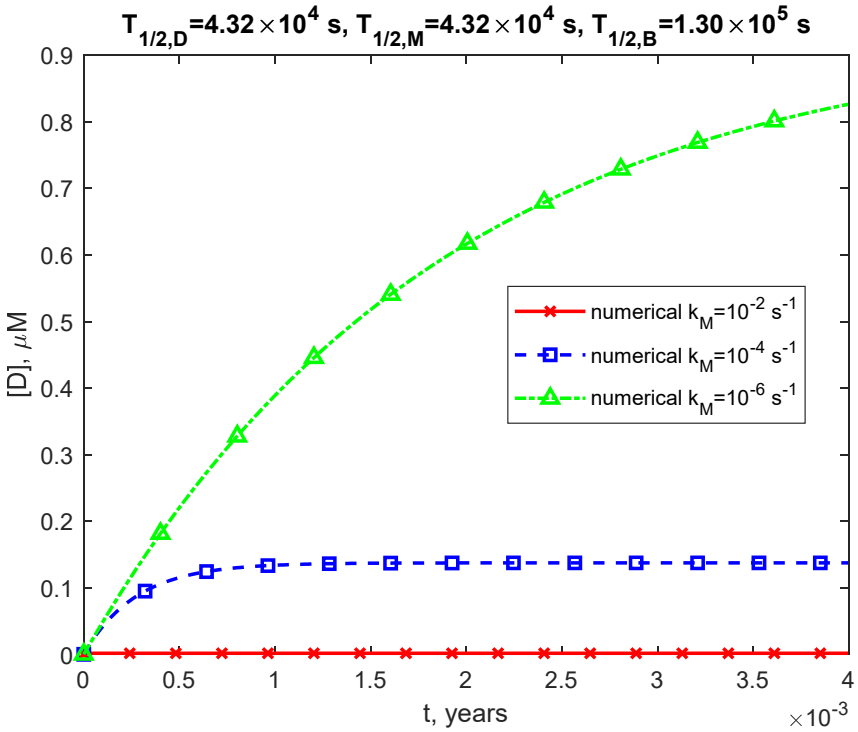

Fig. S16. (a) Molar concentration of TDP-43 dimers, [*D*], over time (in years). (b) Similar to Fig. S16a but focusing on a specific time range of [0 0.004 year] on the *x*-axis. The numerical solution is obtained

by solving Eqs. (4)-(6) numerically with the initial condition (7). The presented scenario assumes physiologically relevant values for the half-lives of TDP-43 dimers, monomers, and aggregates. $T_{1/2,D} = 4.32\times10^4$ s, $T_{1/2,M} = 4.32\times10^4$ s, and $T_{1/2,B} = 1.30\times10^5$ s. The approximate solution is not displayed as it applies exclusively to the scenario involving infinite half-lives of TDP-43 dimers, monomers, and aggregates. The results are displayed for three values of k_M. $k_1 = 10^{-6}$ s^{-1} and $k_2 = 10^{-6}$ μM^{-1} s^{-1}.

(a)

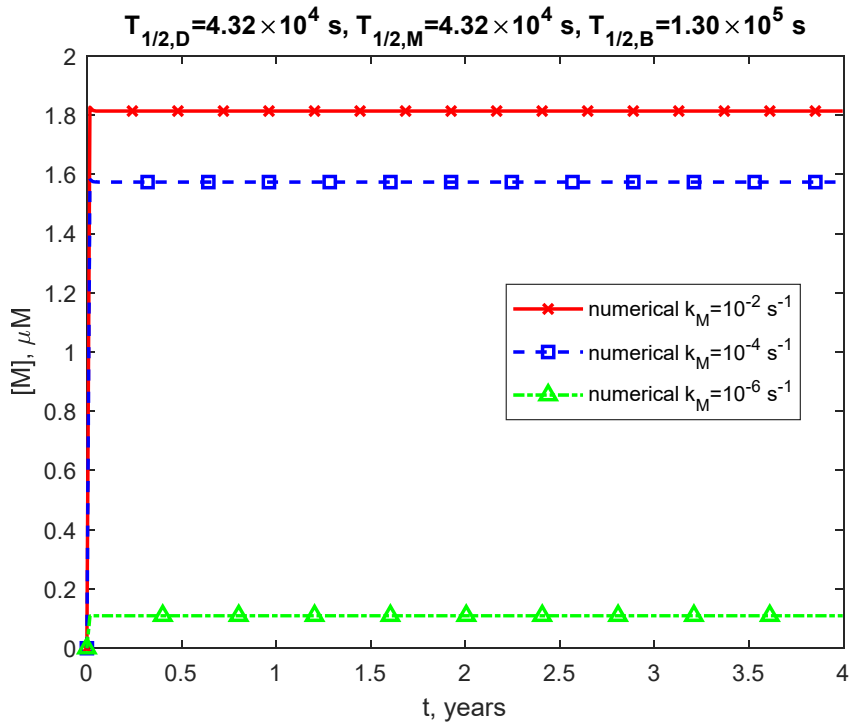

(b)

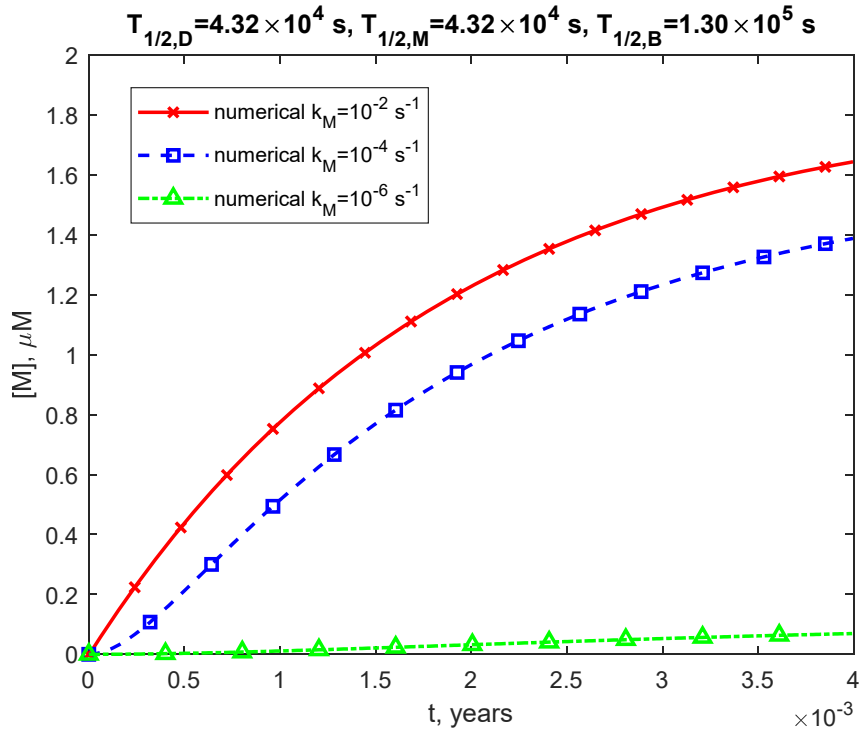

Fig. S17. (a) Molar concentration of TDP-43 monomers, [*M*], over time (in years). (b) Similar to Fig. S17a but focusing on a specific time range of [0 0.004 year] on the *x*-axis. The numerical solution is obtained by solving Eqs. (4)-(6) numerically with the initial condition (7). The presented scenario assumes physiologically relevant values for the half-lives of TDP-43 dimers, monomers, and aggregates. $T_{1/2,D} = 4.32\times10^4$ s, $T_{1/2,M} = 4.32\times10^4$ s, and $T_{1/2,B} = 1.30\times10^5$ s. The approximate solution is not displayed as it applies exclusively to the scenario involving infinite half-lives of TDP-43 dimers, monomers, and aggregates. The results are displayed for three values of k_M. $k_1 = 10^{-6}$ s^{-1} and $k_2 = 10^{-6}$ μM^{-1} s^{-1}.

(a)

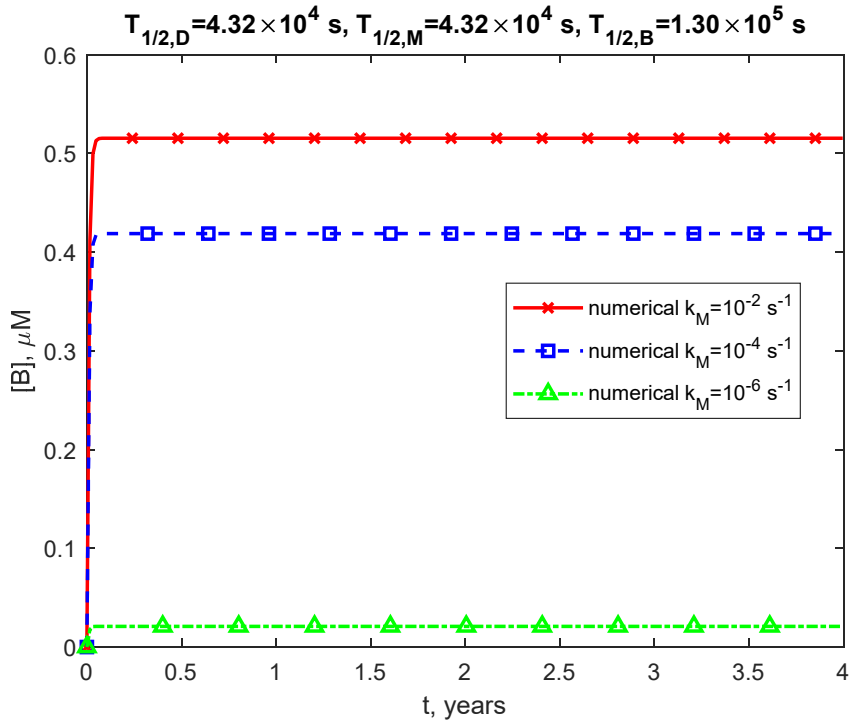

(b)

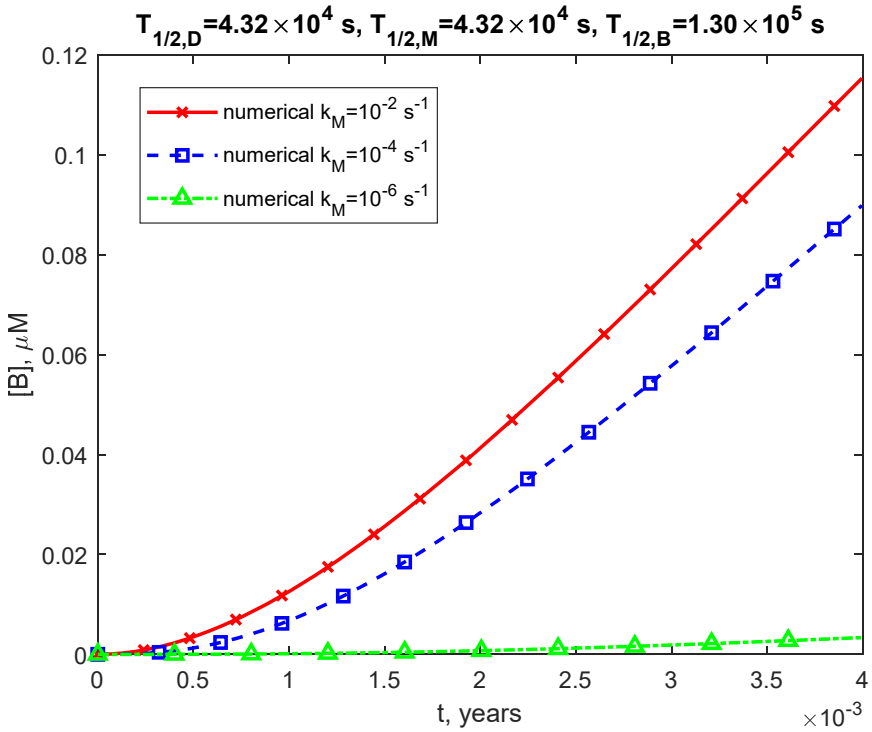

Fig. S18. (a) Molar concentration of TDP-43 aggregates, [*B*], over time (in years). (b) Similar to Fig. S18a but focusing on a specific time range of [0 0.004 year] on the *x*-axis. The numerical solution is

obtained by solving Eqs. (4)-(6) numerically with the initial condition (7). The presented scenario assumes physiologically relevant values for the half-lives of TDP-43 dimers, monomers, and aggregates. $T_{1/2,D} = 4.32 \times 10^4$ s, $T_{1/2,M} = 4.32 \times 10^4$ s, and $T_{1/2,B} = 1.30 \times 10^5$ s. The approximate solution is not displayed as it applies exclusively to the scenario involving infinite half-lives of TDP-43 dimers, monomers, and aggregates. The results are displayed for three values of k_M. $k_1 = 10^{-6}$ s^{-1} and $k_2 = 10^{-6}$ μM^{-1} s^{-1}.